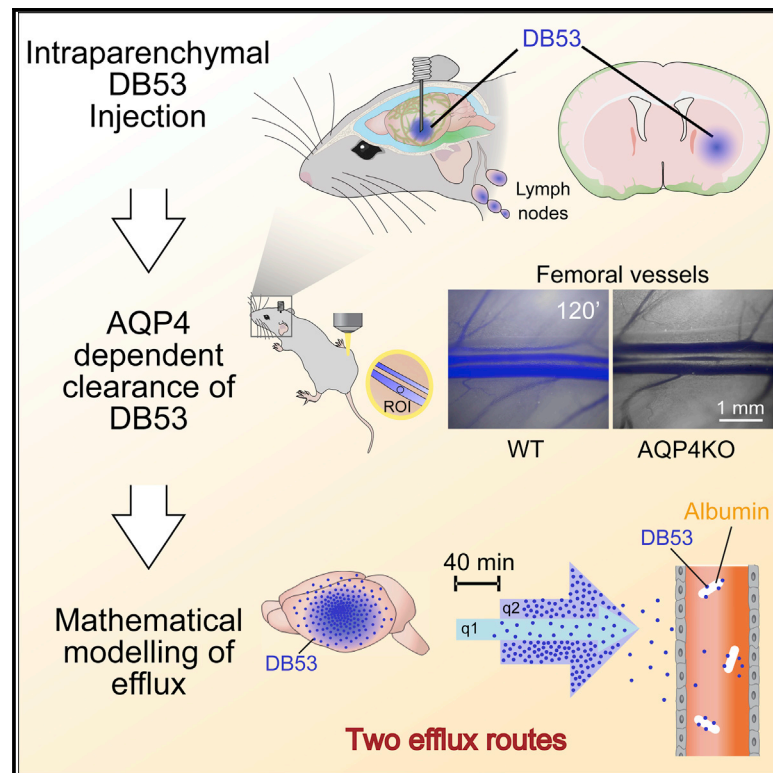


A real-time *in vivo* clearance assay for quantification of glymphatic efflux

Graphical abstract



Authors

Virginia Plá, Peter Bork, Aurakoch Harnpramukul, ..., Douglas H. Kelley, Lauren M. Hablitz, Maiken Nedergaard

Correspondence

maiken_nedergaard@urmc.rochester.edu

In brief

Plá et al. report an *in vivo* methodology that enables the quantification of brain solute outflow under different physiological and pathological states by measuring brain-injected tracer in the vascular compartment. They also develop a pharmacokinetic model of the clearance process, which provides a quantitative tool to study real-time glymphatic clearance.

Highlights

- DB53 assay allows real-time quantification of the glymphatic efflux *in vivo*
- Glymphatic efflux from the parenchyma is dependent on solute size
- Glymphatic solute clearance is AQP4 dependent
- Efflux kinetics are consistent with the existence of at least two efflux routes



Article

A real-time *in vivo* clearance assay for quantification of glymphatic efflux

Virginia Plá,¹ Peter Bork,² Aurakoch Harnpramukul,¹ Genaro Olveda,¹ Antonio Ladrón-de-Guevara,¹ Michael J. Giannetto,¹ Rashad Hussain,¹ Wei Wang,¹ Douglas H. Kelley,³ Lauren M. Hablitz,¹ and Maiken Nedergaard^{1,2,4,*}

¹Center for Translational Neuromedicine, University of Rochester Medical Center, Rochester, NY 14642, USA

²Center for Translational Neuromedicine, University of Copenhagen, 2200 Copenhagen, Denmark

³Department of Mechanical Engineering, University of Rochester, Rochester, NY 14627, USA

⁴Lead contact

*Correspondence: maiken_nedergaard@urmc.rochester.edu

<https://doi.org/10.1016/j.celrep.2022.111320>

SUMMARY

Glymphatic fluid transport eliminates metabolic waste from the brain including amyloid- β , yet the methodology for studying efflux remains rudimentary. Here, we develop a method to evaluate glymphatic real-time clearance. Efflux of Direct Blue 53 (DB53, also T-1824 or Evans Blue) injected into the striatum is quantified by imaging the DB53 signal in the vascular compartment, where it is retained due to its high affinity to albumin. The DB53 signal is detectable as early as 15 min after injection and the efflux kinetics are sharply reduced in mice lacking the water channel aquaporin 4 (AQP4). Pharmacokinetic modeling reveal that DB53 efflux is consistent with the existence of two efflux paths, one with fast kinetics ($T_{1/2} = 50$ min) and another with slow kinetics ($T_{1/2} = 240$ min), in wild-type mice. This *in vivo* methodology will aid in defining the physiological variables that drive efflux, as well as the impact of brain states or disorders on clearance kinetics.

INTRODUCTION

Biological activity generates metabolic waste. In peripheral tissues, waste is exported primarily by the lymphatic system for recycling in the liver or excretion by the kidney (Miller and Inker, 2020; Rabinowitz and Enerbäck, 2020; Vilstrup, 1980). The brain is devoid of lymphatic vessels, and as such clears waste by glymphatic fluid transport (Iliff et al., 2013a; Iliff and Nedergaard, 2013). Our current understanding of brain fluid transport is that cerebrospinal fluid (CSF) enters the glymphatic system along periaxonal spaces, mixes with interstitial fluid in the parenchyma, and exits the brain via multiple routes, including perivascular spaces, arachnoid granulations, cranial and spinal nerves, and meningeal lymphatic vessels, which all drain into the cervical lymphatic vasculature (Benveniste et al., 2017b). Several of the functional and anatomical details of brain fluid transport were already described decades ago (Rennels et al., 1985, 1990). Yet, it was the finding that amyloid- β is cleared by the glymphatic system (Iliff et al., 2012; Peng et al., 2016) that articulated a functional role of brain fluid transport and a renewed interest in the topic (Abbott et al., 2018; Hladky and Barrand, 2014; Rasmussen et al., 2021).

CSF influx along periaxonal spaces *in vivo* has been documented using multiple approaches including two-photon microscopy (Iliff et al., 2012; Kress et al., 2014; Mestre et al., 2018b; Xie et al., 2013), macroscopic transcranial fluorescent imaging (Hablitz et al., 2019, 2020; Kress et al., 2014; Peng et al., 2016), contrast-enhanced MRI (Davoodi-Bojd et al., 2019; Iliff et al., 2013a; Lee et al., 2015; Ringstad et al., 2017, 2018), and

MREG (Kiviniemi et al., 2016). In contrast, little information exists on the pathways and kinetics of efflux of interstitial fluid and solutes. Most studies measure solute clearance from brain by intraparenchymal injection of fluorescent or radioactive tracers followed by quantification of tracer remaining in the brain as a function of time (Cserr et al., 1981; Groothuis et al., 2007; Iliff et al., 2012; Kress et al., 2014; Peng et al., 2016; Xie et al., 2013). This approach requires that the brains of a large number of animals are harvested at discrete time points. Here, we develop a method to assess the kinetics of *in vivo* glymphatic efflux in real-time in individual mice.

Direct Blue 53 (DB53; also named T-1824 or Evans Blue) is a small (960 Da) blood-brain barrier (BBB) impermeable molecule used extensively to assess the integrity of the BBB (Manaenko et al., 2011; Reeve, 1957; Saria and Lundberg, 1983; Saunders et al., 2014, 2015; Wolman et al., 1981). DB53 exhibits low toxicity when used at high concentrations in humans (Dawson et al., 1920; Evans and Schulemann, 1914; Giger et al., 1974). Due to its high water solubility and affinity for albumin (Steinwall and Klatzo, 1966; Wolman et al., 1981; Yen et al., 2013), DB53 remains in the circulation for at least 3 days post injection (Wolman et al., 1981; Yao et al., 2018). DB53 has a fluorescence excitation peak at 620 nm and emission at 680 nm, a range of wavelengths with modest tissue auto fluorescence. Thus, the DB53 signal can be detected *in vivo* in blood vessels with a high signal-to-noise ratio.

Here, we introduce a methodology that quantifies the kinetics of DB53 efflux from the brain parenchyma by continuous measurement of DB53 signal in the periphery (femoral vein). This



approach enables the quantification of total DB53 efflux from the parenchyma *in vivo* in a single animal, avoiding postmortem artifacts and sharply reduces the number of animals needed to establish the temporal kinetics of glymphatic clearance. We use this technique to test how the molecular size of the tracer may restrict export from the brain and test the importance of the water channel aquaporin 4 (AQP4) in DB53 efflux kinetics. Pharmacokinetic modeling of the data provides insights into the basic principles underlying brain clearance.

RESULTS

DB53 exhibits a dose-dependent and stable signal in the vascular compartment

Pilot experiments showed that imaging of the exposed femoral vein provided the highest DB53 signal relative to background (tissue autofluorescence) compared with other vessels, such as the tail vein. To evaluate the sensitivity of the clearance assay, the DB53 fluorescent signal was first quantified at the femoral vein using a slow rate of infusion (intravenously [i.v.], 0.2 $\mu\text{L}/\text{min}$, 15 min), capturing an image every 5 min (Figure S1A). The DB53 signal was detectable after injection of 1 μL DB53 (+218% from baseline, Figures S1B and S1C; Table S4) corresponding to ~ 0.6 $\mu\text{g}/\text{mL}$ DB53 in venous blood. The stability of the DB53 signal was evaluated by i.v. delivery (3.0 μL , 0.1% [w/v] bolus injection) through the contralateral femoral vein (Figure S1D). Baseline fluorescence ($t = 0$ min) was comparable across all animals (Table S2). The DB53 signal reached maximum value in less than 1 min and remained constant during the 120 min imaging period ($t = 30$ min: 128.3 ± 41.8 a.u.; $t = 135$ min: 142.3 ± 36.8 a.u., Figures S1D and S1E; Table S4), consistent with previous studies that have shown that the DB53 signal is stable in blood (Connolly and Wood, 1954; Yao et al., 2018). We also compared i.v. injection of DB53 with a polymeric tracer (fluorescein poly(ethylene glycol) [FITC-PEG] 1 kDa) that is biologically inert and does not bind albumin (Roberts et al., 2002). Both DB53 and FITC-PEG are detected in the vascular compartment after i.v. injection, but FITC-PEG is rapidly cleared from blood by kidney filtration and is therefore unusable as a glymphatic clearance tracer (Figures S2A–S2E). These studies showed that DB53 is detected in the vascular compartment with high sensitivity, where it remains stable for hours after injection.

DB53 freely distributes within the brain parenchyma

Unbound DB53 is relatively small (960 Da). This, combined with the near absence of albumin in the brain parenchyma (Spector et al., 2015), should allow DB53 to move freely in the brain. To test this, we compared parenchymal distribution of DB53 with FITC (389 Da), which is freely diffusible (Bedussi et al., 2015; Binder et al., 2004; Naessens et al., 2021; Nicholson and Sykova, 1998; Nicholson and Tao, 1993; Simmons et al., 2018). DB53 and FITC (both 0.25%) were co-injected via a micro-cannula in the striatum (1 μL , 0.2 $\mu\text{L}/\text{min}$). Tracers were dispersed for 20 min before the brain was rapidly harvested after decapitation (<2 min), followed by preparation of vibratome sections and imaging to map the regional distribution of FITC and DB53 (Figure 1A). No significant differences were noted between DB53

and FITC dispersion (Figure 1C, FITC: $8.9\% \pm 1.0\%$ area, DB53: $6.5\% \pm 3.4\%$ area, Table S1), or their radial distribution from the injection site (Figure 1D, FITC: 82.0 ± 14.5 area, DB53: 68.6 ± 15.3 a.u., Table S1). These data support the conclusion that DB53 diffusion is unrestrained in the brain parenchyma.

Optimizing the clearance assay to limit impact on glymphatic, glial, and neuronal function

Acute unilateral cannula implantation has been shown to suppress global CSF transport (Mestre et al., 2018a). To control for the undesirable effect on brain fluid transport, we systematically tested whether increasing the time between cannula implantation and the clearance assay would recover glymphatic function. Mice were implanted with intrastriatal cannulas, then received a cisterna magna (CM) injection of FITC-conjugated 10 kDa Dextran (0.5%, 10 μL , 2 $\mu\text{L}/\text{min}$) (Xavier et al., 2018) immediately following, and 2, 24, or 72 h post implantation to measure glymphatic influx. The brains were harvested 30 min after FITC injection, processed, and total tracer amounts within the brains were compared (Figures 2A and 2B).

We found no difference in tracer influx after anesthesia for 30 min or 2.5 h, indicating that the duration of the procedure does not interfere with glymphatic function (30 min: 23 ± 2 a.u.; 2.5 h: 22 ± 4 a.u., Figure 2C; Table S2). Regional analysis of tracer distribution revealed that there was no differential effect on glymphatic influx between contralateral or ipsilateral sides of the brain injection sites when comparing data across the groups (Figure 2D). In addition, the ratio of CSF tracer distribution between non-implanted and implanted side was close to 1, showing that acute, unilateral cannula insertion induced a global suppression of the glymphatic system rather than a regional effect (Figure 2E). Neither aCSF nor DB53 parenchymal infusion (4%, 1 μL , 0.2 $\mu\text{L}/\text{min}$) 24 h after cannula implantation significantly reduced CSF tracer influx compared with controls (aCSF: 24 ± 2 a.u.; DB53: 21 ± 4 a.u.). Finally, the time gap between the striatal cannula implantation and DB53 clearance had significant effects on glymphatic function. Acute cannula implantation reduced glymphatic CSF tracer influx to as low as 27% of controls (acute: 6 ± 1 a.u., Figure 2C). After 24 h, glymphatic CSF tracer transport recovered to control (non-implanted) levels and remained at control levels 72 h post cannula implantation (24 h recovery: 21 ± 1 a.u.; 72 h recovery: 22 ± 2 a.u., Figure 2C).

Glymphatic influx was strongly suppressed acutely after cannula implantation but recovered to baseline levels at 24 or 72 h post cannula implantation (Figure 2D). However, cannula placement can cause glial scarring, which has been reported to change the extracellular space volume and tortuosity (Sykova and Nicholson, 2008). We assessed astrocytic and microglial reactivity by immunolabeling against GFAP and Iba1, respectively, in brains harvested at 24 and 72 h post implantation, and non-surgical controls (Figure S3). The global expression of GFAP and Iba1 was slightly increased at 24 h, and further elevated at 72 h post surgery. We found no increase in percent area of GFAP immunoreactivity between the cortex (CX) close to the injection site and the lateral ventricles after 24 h (Figures S3B and S3C; Table S4). At 72 h post implantation GFAP expression was increased in CX (Figures S3B and S3C;

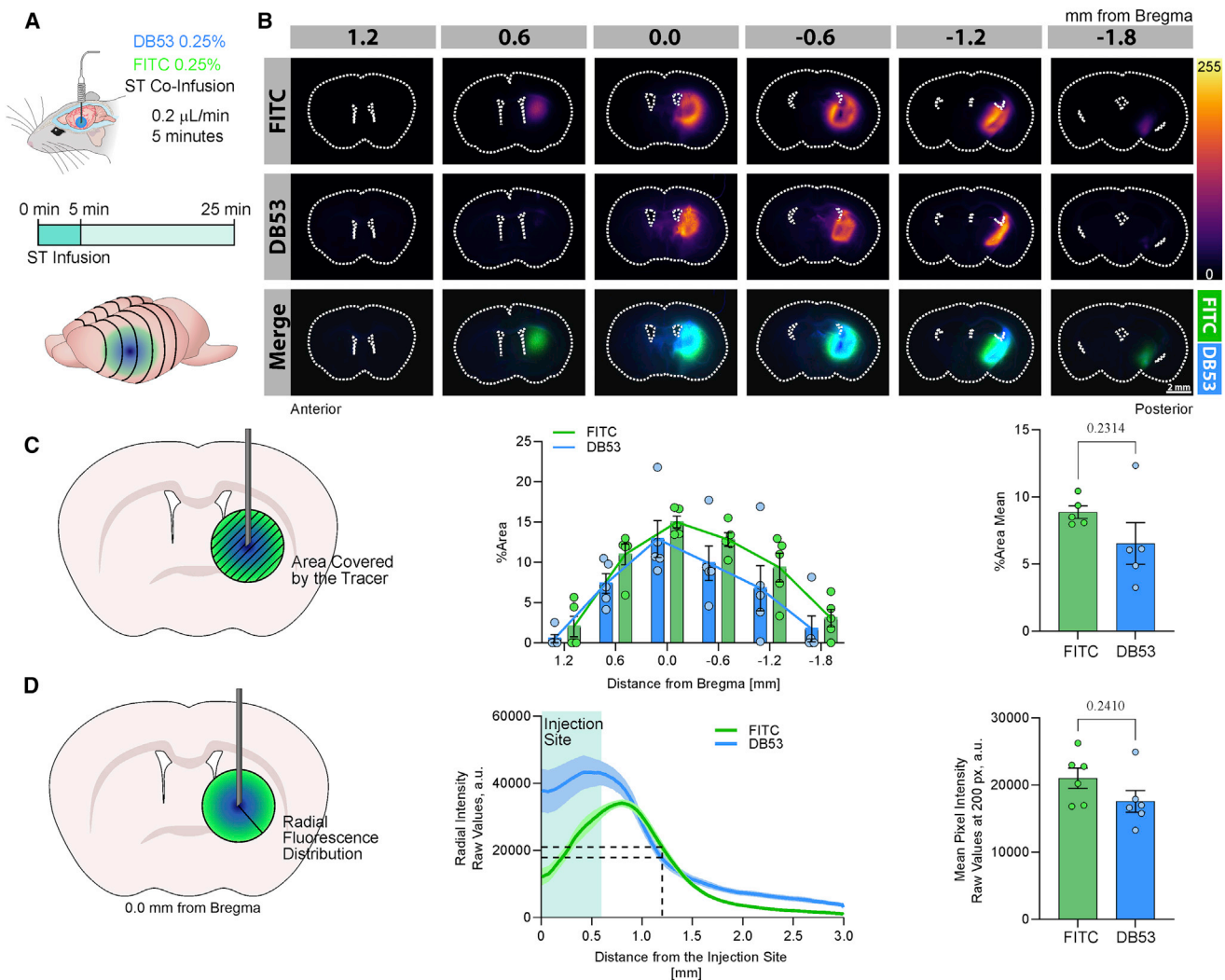


Figure 1. DB53 diffuses freely in the brain parenchyma

(A) Experimental design. Animals were co-injected with FITC and DB53 (0.25% [w/v], 1 μ L, 0.2 μ L/min), and the brains harvested 20 min later, freshly sliced, and imaged.

(B) Representative slices showing FITC signal (upper panel and green) and DB53 signal (middle panel and blue). Numbers indicate the anteroposterior distance from bregma in mm.

(C) Quantification of percent area covered by the tracers per slice (center) and mean (right). Six slices per animal were analyzed, and each animal was considered a biological replicate. Bars are average with SEM. Individual values are shown. Numbers indicate the anterior/posterior distance from bregma in mm.

(D) Radial analysis of fluorescence distribution along the ipsilateral side of slices at 0.0 mm from bregma, normalized by the maximum fluorescence values at the injection point (center). The right-hand graph shows the percent of initial fluorescence at 600 μ m from the origin (approximately half of the distance traveled by the tracers) showing mean \pm SEM.

* $p < 0.05$, ** $p < 0.01$, *** $p < 0.001$, **** $p < 0.0001$. ST, striatum; a.u., arbitrary units. $n = 5$.

Table S4). Iba1 expression was increased at 72 h in ipsilateral CX and striatum compared with controls (Figures S3D and S3E; Table S4), with no significant differences in the contralateral side compared with control animals (Figures S3D and S3E; Table S4), indicating an injury-specific response (Benveniste and Diemer, 1987; Kozai et al., 2015; Wellman and Kozai, 2017). Based on these data, we conclude that reactive changes in response to cannula placement peaks at 72 h. Importantly, DB53 infusion did not induce additional glial reactivity in the injection area (Figure S4).

DB53 toxicity has been noted in *in vitro* assays or *in vivo* at extremely high doses (≥ 50 mg/kg) during prolonged exposure times in the range of days or months. To test for potential acute neurotoxicity, we measured cortical electrical activity via electroencephalography (EEG) before and after injection of DB53. EEG power spectra exhibited no changes after injection of either aCSF or DB53 compared with baseline (Figure S5), indicating that DB53 injection does not affect neural activity. These findings are consistent with the literature reporting that administration of DB53, under a variety of doses and delivery routes, is not

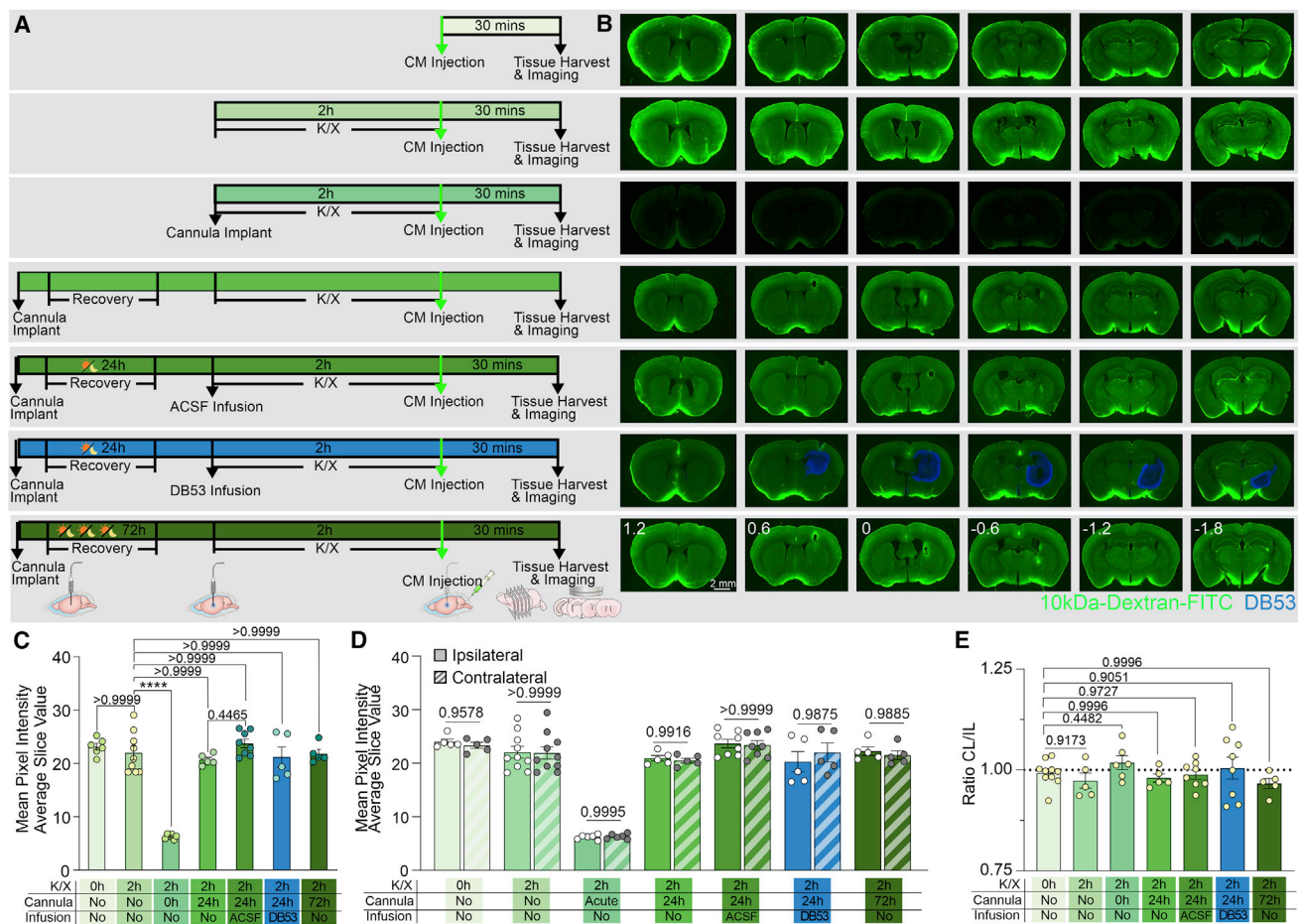


Figure 2. Impact of intrastriate cannula implantation on the glymphatic system

(A) Experimental design. CM injections (0.5% [w/v] in aCSF, 10 kDa-dextran-FITC, 10 μ L, 2 μ L/min, 30 min of circulating time) were performed to evaluate effects of K/X anesthesia, cannula implantation, and injection of vehicle or DB53. Seven experimental groups were defined.

(B) Representative slices showing influx (green) and DB53 (blue) in all experimental groups. Numbers indicate the anterior/posterior distance from bregma in mm.

(C) FITC fluorescence: mean pixel intensity quantification in arbitrary units of six slices per animal.

(D) Graph showing mean pixel intensity quantification of IL (solid) and CL (lined) sides of each slice.

(E) Ratio CL/IL was shown to evaluate differences between each side. Graphs show mean \pm SEM and individual values, with each point corresponding to one animal. Significance ascribed as: * $p < 0.05$, ** $p < 0.01$, *** $p < 0.001$, **** $p < 0.0001$. ST, striatum; CL, contralateral; IL, ipsilateral; AP, anteroposterior; a.u., arbitrary units.

$n = 6, 9, 6, 5, 8, 5$, and 5.

associated with toxicity *in vivo*. We conclude that the intrastriate DB53 injection paradigm as used here is not associated with any signs of acute or chronic neurotoxicity.

Dose dependency of the DB53 clearance assay

We next tested the sensitivity and reproducibility of intrastriate DB53 injection. Three different infusion volumes of DB53 (4% [w/v]; 0.2 μ L/min): 0.5, 1.0, and 1.5 μ L were injected into striatum 24 h after cannula placement (Figure 3A). Percent area of DB53 within brain slices was directly proportional to the injected volume of DB53 (Figures 3B and 3C). Anterior/posterior fluorescence signal distribution in brain slices showed analogous patterns of diffusion of DB53 at all infusion volumes, with peak intensity in the slice with the probe (Figure 3D). In the femoral

vein, the DB53 signal was detectable at all concentrations and as early as 15 min after injection in the 1.5 μ L group (Figure 3E). At 120 min, the DB53 signal was significantly higher with increased injected volume (Figure 3F; Table S1). The skin opening did not affect the signal detected over the femoral vein. We also compared injection of DB53 and PEG to test whether clearance to the vascular compartment was tracer specific (Figures S2F and S2G). Both DB53 and PEG exhibited higher signals in the vascular compartment at 2 h, although the magnitude of change was less in the PEG group, most likely due to PEG clearance by the kidney (Figure S2E) (Brady et al., 1986). We conclude that intra-parenchymal DB53 injection is reliable, reproducible, and can be detected in the periphery in a dose- and time-dependent manner.

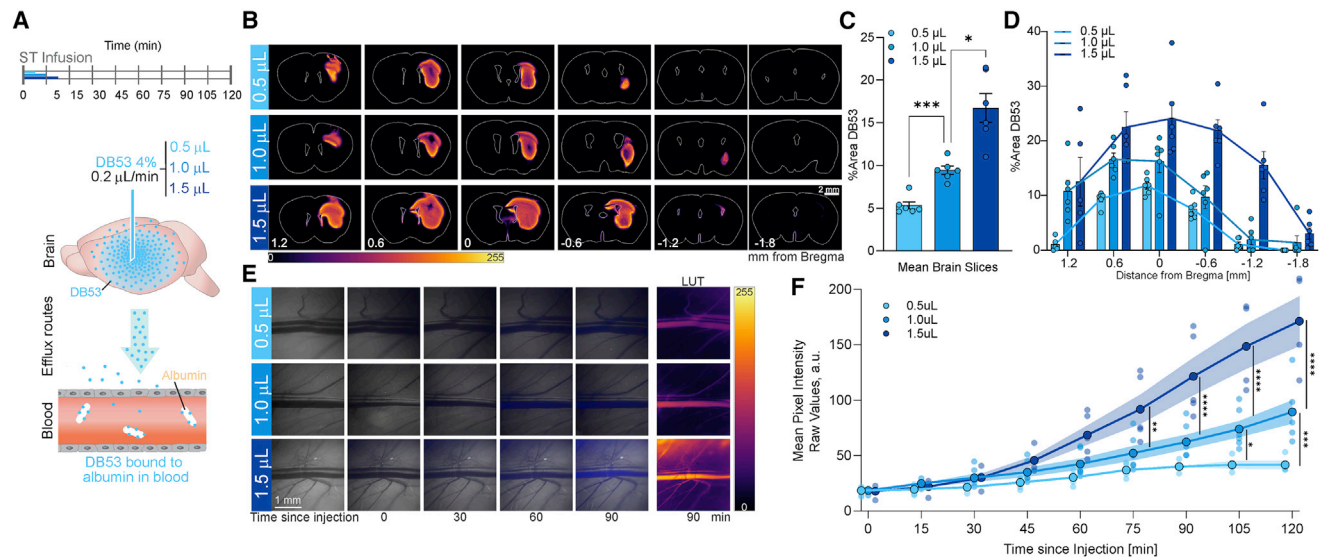


Figure 3. Efflux of intrastriate-injected DB53

(A) Scheme of the performed experiments. Injecting paradigms used: 0.5, 1.0, and 1.5 μL , 0.2 $\mu\text{L}/\text{min}$.

(B) Representative slices showing the DB53 signal in the brain at the end of the experiment. The anterior/posterior distance from bregma in millimeters is indicated.

(C) Graph showing the quantification of the percent area covered by DB53 after different volume injections of 4% DB53 in the brain. Bars show mean with SEM. Individual animals are shown as dots.

(D) The anterior/posterior distribution of DB53 covered by mean percent area for the three injected volumes.

(E) Representative images of the acquired *in vivo* femoral vein images. Pseudocolor for 90 min images shown for clarity.

(F) Quantification of the mean pixel intensity fluorescence, corresponding to the different injected volumes. Graph showing solid lines for mean values with SEM shown as shading. Individual animals are shown as semitransparent circles. * $p < 0.05$, ** $p < 0.01$, *** $p < 0.001$, **** $p < 0.0001$.

(C), (D), (G), and (H), $n = 6$ (0.5 μL), 6 (1.0 μL), and 8 (1.5 μL).

Glymphatic efflux from the parenchyma is dependent on solute size

Diffusive transport of solutes through the parenchyma is highly dependent on molecular size (Nicholson and Sykova, 1998; Rusakov and Kullmann, 1998; Sykova and Nicholson, 2008). To test how this impacts the clearance assay, DB53 (40 $\mu\text{g}/\mu\text{L}$ in aCSF) was incubated with bovine serum albumin (BSA)-enriched solution (400 $\mu\text{g}/\mu\text{L}$ in aCSF) (Figure 4A). Final concentrations of DB53 in the DB53–BSA conjugated solution was comparable with the free DB53 solution (DB53–BSA: $47.2 \pm 5.8 \mu\text{g}/\mu\text{L}$; free DB53: $45.4 \pm 6.9 \mu\text{g}/\mu\text{L}$, Figure 4A). Free DB53 or DB53+BSA were then injected into the striatum (0.2 $\mu\text{L}/\text{min}$, 5 min) (Figure 4B). The mean percent area covered across the coronal slices at the end of the experiment was larger in the DB53+BSA group (Figures 4C and 4D, free DB53: $9.3\% \pm 1.3\%$; DB53+BSA: $18.75\% \pm 0.3\%$; Table S2). There were no significant differences in distribution along the antero-posterior axis at 15 min post injection (Figures S6A and S6B). At 120 min post injection, DB53+BSA covered a larger area, but with a lower signal intensity than DB53 (Figure S5B). These observations may reflect that the larger molecule (DB53+BSA) remains longer in the brain parenchyma while the smaller molecule (DB53) is cleared faster.

The amount of DB53 remaining in the tissue was quantified after formamide extraction (Graesser et al., 2002; Katayama et al., 1978; Radu and Chernoff, 2013) to assess the dynamics of DB53 and DB53+BSA in the brain. While free DB53 decreased in the brain between 10 and 120 min after injection, there was no significant

change in the DB53+BSA in the brain (Figure 4E). In addition, there was almost no efflux of DB53+BSA to the vascular compartment after the intrastriate infusion compared with free DB53 (Figures 4F–4H, free DB53: 68.2 ± 15.8 a.u., DB53+BSA: 23.5 ± 1.8 a.u., Table S2). Finally, only plasma concentration of free DB53 significantly increased at the end of the experiment (Figure 4I, free DB53: $1.6 \pm 0.4 \mu\text{g EB}/\text{mL}$ plasma; DB53+BSA: $0.1 \pm 0.1 \mu\text{g EB}/\text{mL}$ plasma, Table S2), and only free DB53 was found in the lymph nodes (Figures 4J and 4K). Taken together, these observations support the hypothesis that conjugated DB53+BSA exhibited decreased efflux, and that the molecular size of the tracer impacts its clearance.

To further evaluate the importance of tracer size on brain clearance, a mixture of PEG with distinct molecular weight was infused in the parenchyma (4% each of, PEG 1 kDa-FITC and PEG 40 kDa-Rhodamine, 1 μL total, 0.2 $\mu\text{L}/\text{min}$, striatum). Biologically inert PEGs were used to minimize the interactions of the tracers with brain (Hamidi et al., 2006; Pelham et al., 2008). There was no difference in tracer recovery from the brains immediately after injection compared with the equivalent amount of tracer in formamide or in brain homogenate, confirming the efficacy of formamide extraction in determining PEG concentrations after brain injection (Figures 4M and 4N). Quantification of brain PEG content at different time points (1, 4, 18, and 28 h from injection) showed that only FITC-PEG 1 kDa was cleared from the brain, while Rhodamine-PEG 40 kDa content remained constant for the entire experiment, supporting the existence of a size-specific barrier to brain efflux.

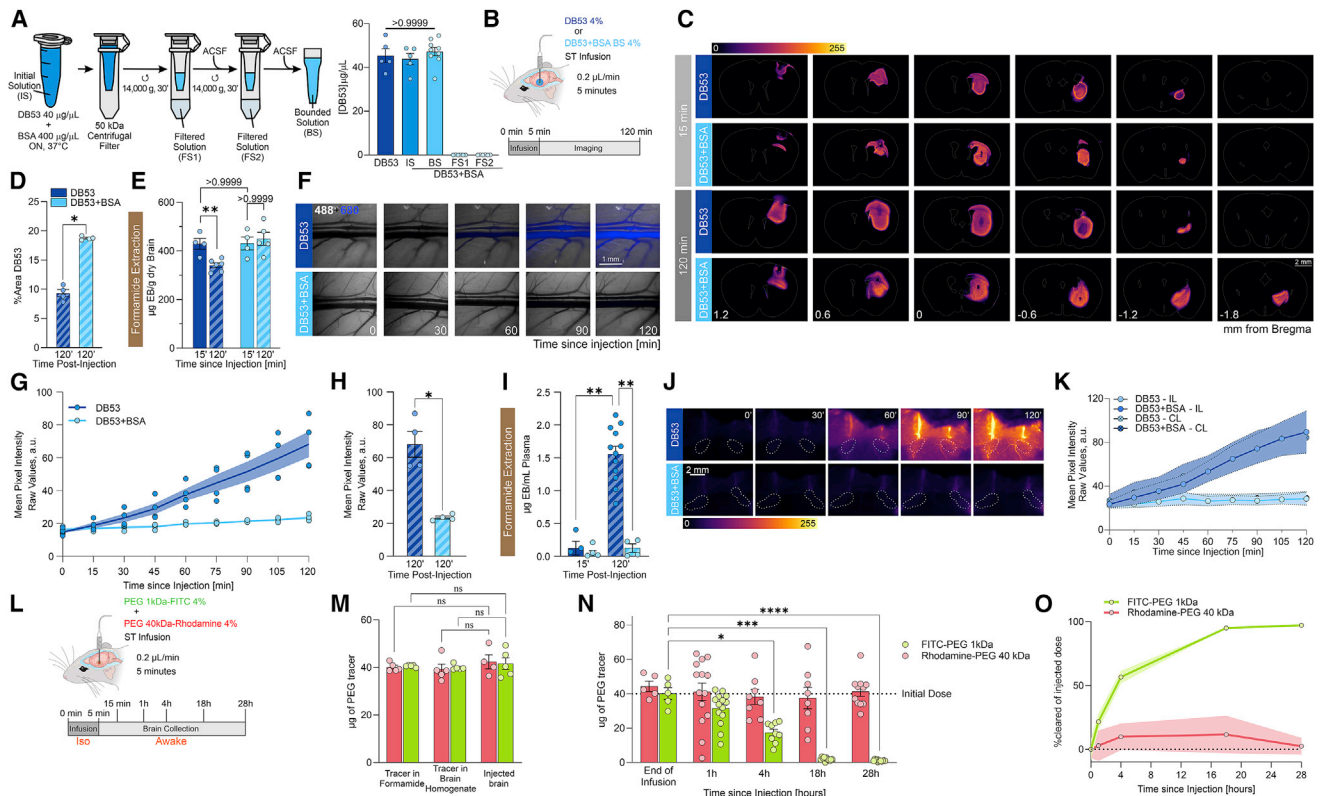


Figure 4. DB53 clearance from brain is size dependent

(A) Scheme of the preparation of high and low molecular forms of DB53. Graph showing the quantification of the concentration of the DB53 in the different solutions used, either free DB53, or DB53 bound to BSA (DB53+BSA). Dots are replicates in the spectrophotometric measurements; error bars indicate SEM.

(B) Scheme of the experimental design. Free DB53 or DB53 bound to BSA is injected and clearance to blood measured for 120 min. Brains are then harvested to quantify remaining solutes.

(C) Representative slices showing the DB53 signal in the brain at $t = 15$ and 120 min. The AP distance from bregma in mm is indicated.

(D) Graphs showing the percent area covered by DB53 after injections of 4% DB53 or DB53+BSA in the brain. Bars show mean with SEM, individual animals shown as dots, six slices per animal.

(E) Brain spectrophotometric quantification of the DB53 content at 120 min after extraction by formamide. Bars show mean with SEM of analyzed samples, individual animals as dots.

(F) Representative images of the *in vivo* femoral vein images after intrastriatal injection of 4% DB53 or DB53+BSA.

(G) Quantification of the mean pixel intensity fluorescence in the femoral vein, corresponding to the free DB53 or DB53+BSA infusions. Graph showing mean with SEM, each colored point corresponds to one animal.

(H) Fluorescence values in the femoral vein at the end of the experiment ($t = 120$ min) for both tracers.

(I) Spectrophotometric quantification of the DB53 content in plasma at 120 min by formamide extraction. Bars summarize mean with SEM of analyzed samples corresponding to one animal, marked as dots.

(J) Representative *in vivo* images of the cervical lymph nodes after intrastriatal DB53 or DB53+BSA infusion.

(K) Quantification of the mean pixel intensity in the superficial cervical lymph nodes is shown on the right (mean with SEM).

(L) Scheme of the experimental design. Equal amounts of FITC-PEG 1 kDa and Rhodamine-PEG 40 kDa were injected, and brains harvested at varying time points.

(M) Quantification of the tracer recovery from solutions containing the full dose of tracer mix (40 μ g each, FITC-PEG 1 kDa and Rhodamine-PEG 40 kDa) in formamide, in brain homogenate, and after intrastriatal injection into the brain at $t = 15$ min (end of infusion). Each dot is an individual animal, bars show average with SEM.

(N) Quantification of the brain content at the different time points (end of infusion, and at 1, 4, 18, and 28 h). Bars show mean with SEM, each dot is an individual animal.

(O) Line graph summarizing the mean tracer content change along the time course for both tracers. Shaded area is SEM. * $p < 0.05$, ** $p < 0.01$, *** $p < 0.001$, **** $p < 0.0001$.

(D)–(I) $n \geq 4$; (K)–(O) $n \geq 5$. BS, albumin-bound DB53; IS, initial solution; FS1 and FS2, filtered solutions 1 and 2; BS, albumin-bound DB53; BSA, bovine serum albumin; CTR, control; DCLN, deep cervical lymph nodes; SCLN, superficial cervical lymph nodes.

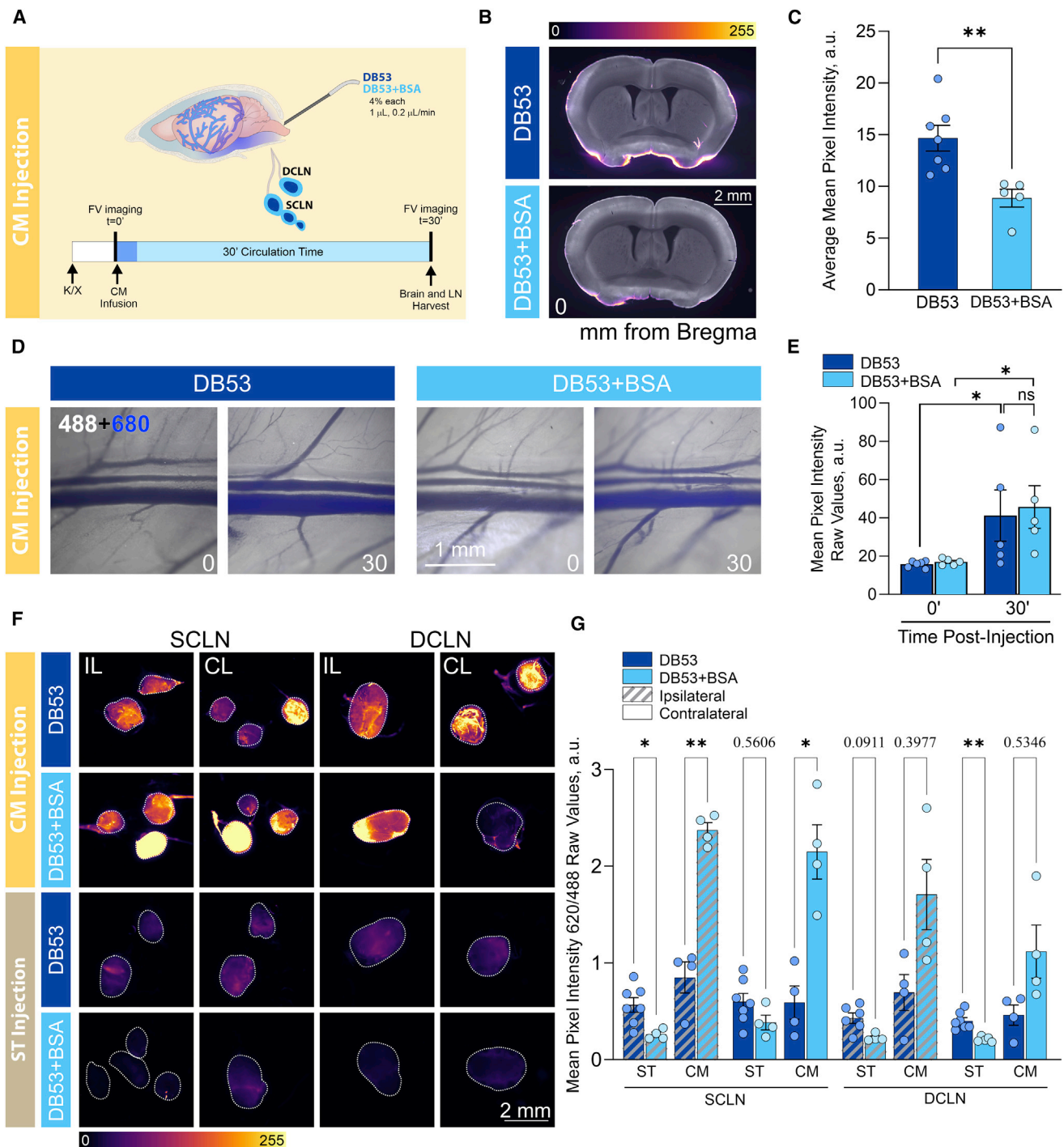


Figure 5. DB53 efflux from CSF to peripheral lymphatic nodes is independent of molecular weight

(A) Scheme of the experimental design. DB53 or DB53 bound to BSA (DB53+BSA) is infused in the cerebrospinal fluid via the cisterna magna. At 30 min post infusion, tracer is quantified in femoral vein, brain, and lymph nodes.

(B) Representative images of brain slices after CM injection (1 μ L, 0.2 μ L/min) after 30 min of circulation time for 4% DB53 or DB53+BSA.

(C) Graph showing mean pixel intensity averaged from six representative slices per animal. Bars show mean with SEM. Individual animals are shown as dots.

(D) Representative images from the femoral vein before the infusion and at 30 min post injection of the tracer.

(E) Quantification of the mean pixel intensity fluorescence in the femoral vein, corresponding to the free DB53 or DB53+BSA solutions. Graph showing mean \pm SEM, each colored point corresponds to one animal.

(legend continued on next page)

Efflux of solute from the CSF in the CM is fundamentally different than from the parenchyma

One potential caveat of the intrastriate delivery of DB53 is that the tracer is injected directly into the lateral ventricles and thereby reaches the blood compartment by CSF efflux. To critically assess this possibility, we compared the efflux kinetics of DB53 injected either in the striatum or in the lateral ventricle. DB53 reached the blood compartment faster and at higher concentrations after ventricular injection (Figure S7), highlighting the differences in clearance of tracer from the brain compared with clearance from the skull.

We then asked whether the size dependency of solute distribution was a general feature of CSF efflux from the skull, or specific to efflux from the parenchyma by injecting DB53 or DB53+BSA into CM. The analysis revealed a size-dependent difference of glymphatic influx into coronal sections of free DB53 compared with DB53+BSA (Figures 5A–5C, free DB53: 14.7 ± 3.3 a.u.; DB53+BSA: 8.9 ± 1.9 a.u., Table S2), consistent with previous reports (Iliff et al., 2012). The DB53 signal in the vascular compartment was 4× higher than after intrastriate injection, yet exhibited no significant differences after 30 min of circulation (Figures 5D and 5E, free DB53: 40 ± 29 a.u.; DB53+BSA: 44 ± 24 a.u., Table S2). *Ex vivo* fluorescence analysis of the cervical lymph nodes showed a significantly larger accumulation of DB53+BSA than free DB53 (Figures 5F and 5G, free DB53: 0.8 ± 0.4 a.u.; DB53+BSA: 1.6 ± 0.6 a.u., Table S2), likely reflecting that larger molecular weight compounds are more likely to be trapped in lymph nodes than smaller compounds that are washed out (Clement et al., 2018; Rasmussen et al., 2021). We conclude that CSF efflux routes from the skull to the vasculature are much faster and do not have the same size-exclusion principles as efflux from the brain.

Glymphatic solute clearance is AQP4 dependent

The water channel AQP4 facilitates glymphatic fluid transport (Iliff et al., 2012, 2014; Mestre et al., 2018a). Previous studies have documented that deletion of AQP4 sharply decreased glymphatic clearance. In these studies, the tracers were injected in the striatum, frontal CX, or lateral ventricle (Iliff et al., 2012; Lundgaard et al., 2017; Murlidharan et al., 2016) and clearance quantified as brain tracer content as a function of time after injection. We next used the dependence of brain clearance on AQP4 to validate the DB53 assay. Intrastriate DB53 clearance in AQP4 knockout (AQP4KO) mice and littermate wild-types (WT) was compared. The analysis showed that DB53 signal in the femoral vein was sharply reduced in the AQP4KO group compared with the WT after intrastriate DB53 injection (1 μ L), with AQP4KO mice exhibiting 50% less signal at 2 h compared with WT mice (Figure 6, WT: 91.4 ± 30.9 a.u.; AQP4KO: 45.2 ± 17.7 a.u., Table S2). There were no significant differences in the diameter

of the femoral vein and artery (data not shown), mean arterial pressure (data not shown), intracranial pressure (Figure S8), or brain distribution of DB53 in the parenchyma (Figures 6D and 6E, WT: $9.7\% \pm 1.2\%$ area; AQP4KO: $11.6\% \pm 2.8\%$ area, Table S2) between the groups during the experiment, supporting the hypothesis that DB53 clearance is reduced in AQP4KO mice due to a decline in glymphatic function. Thus, these findings confirm and extend previous studies reporting that glymphatic clearance is AQP4 dependent, and concurrently validate the DB53 assay.

Efflux kinetics are consistent with the existence of at least two efflux routes

We next used pharmacokinetic modeling (Roselli and Diller, 2011) of the data generated by this new, *in vivo* glymphatic clearance assay to better understand how efflux changes over time. The simplest pharmacokinetic model would assume that the total mass of DB53 is constant and well-mixed, and that efflux occurs via a single transport mechanism with a constant rate. That model would predict that DB53 concentration in the blood increases most rapidly immediately after injection, then decelerates asymptotically to a final concentration after a long time period. However, 0.5 μ L injections (Figure 3F) of DB53 show efflux accelerating at early times and decelerating at later times, which suggests that the efflux mechanisms are more complex.

A modified pharmacokinetic model better fitted the experimental data, where instead of a single clearance mechanism we assume the existence of two separate rates of clearance: DB53 is transported from brain to blood slowly at first, with an additional, faster transport mechanism activated when the tracer reaches a tissue boundary at time t_0 (Figure 7). Based on these assumptions, we arrived at a four-parameter mathematical model (see STAR Methods). Fitting to the measurements, we find the model coefficient of variation is $R^2 > 0.99$ in all treatment groups (all injection volumes: Figure 7). Using the 0.5 μ L injection group, where DB53 reaches sufficiently stable levels for parameter estimates to be reliable, the slow route alone would reduce blood levels of DB53 to half their steady value in $T_{1/2} = 240$ min, while the fast route activates after $t_0 = 40$ min and alone would produce half the stable blood levels in $T_{1/2} = 50$ min. The fact that neither route is sufficient to describe the data alone supports our hypothesis that both routes must be active to explain the kinetics of DB53 clearance.

Next, we applied the four-parameter model to the AQP4KO mice. The second route started similar to WT mice after $t_0 = 30$ min, consistent with the existence of two routes of glymphatic efflux. However, the first and second rates of transport were now much slower, with $T_{1/2} = 15$ –17 h ($R^2 = 0.986$, Figure 7), which is consistent with impaired glymphatic clearance in AQP4KO mice.

(F) Representative images of the *ex vivo* lymph nodes at the end of the circulation time (30 min for CM and 120 min for ST injection). Ipsilateral and contralateral sides are indicated to allow comparison.

(G) Fluorescent mean pixel intensity for each lymph node normalized by the autofluorescence at 488 nm at the end of the experiment for both conditions (striatal or cisterna magna infusion). Fluorescence values for lymph nodes were averaged for each animal. Graph shows mean with SEM and dots are individual animals. * $p < 0.05$, ** $p < 0.01$, *** $p < 0.001$, **** $p < 0.0001$.

(B)–(D) $n \geq 5$, (F) $n \geq 3$. DB53+BSA, albumin-bound DB53; BSA, bovine serum albumin; CM, cisterna magna; DCLN, deep cervical lymph nodes; IL, ipsilateral; CL, contralateral; ST, striatum; SCLN, superficial cervical lymph nodes. (C) and (G) $n \geq 4$; (E) $n \geq 5$.

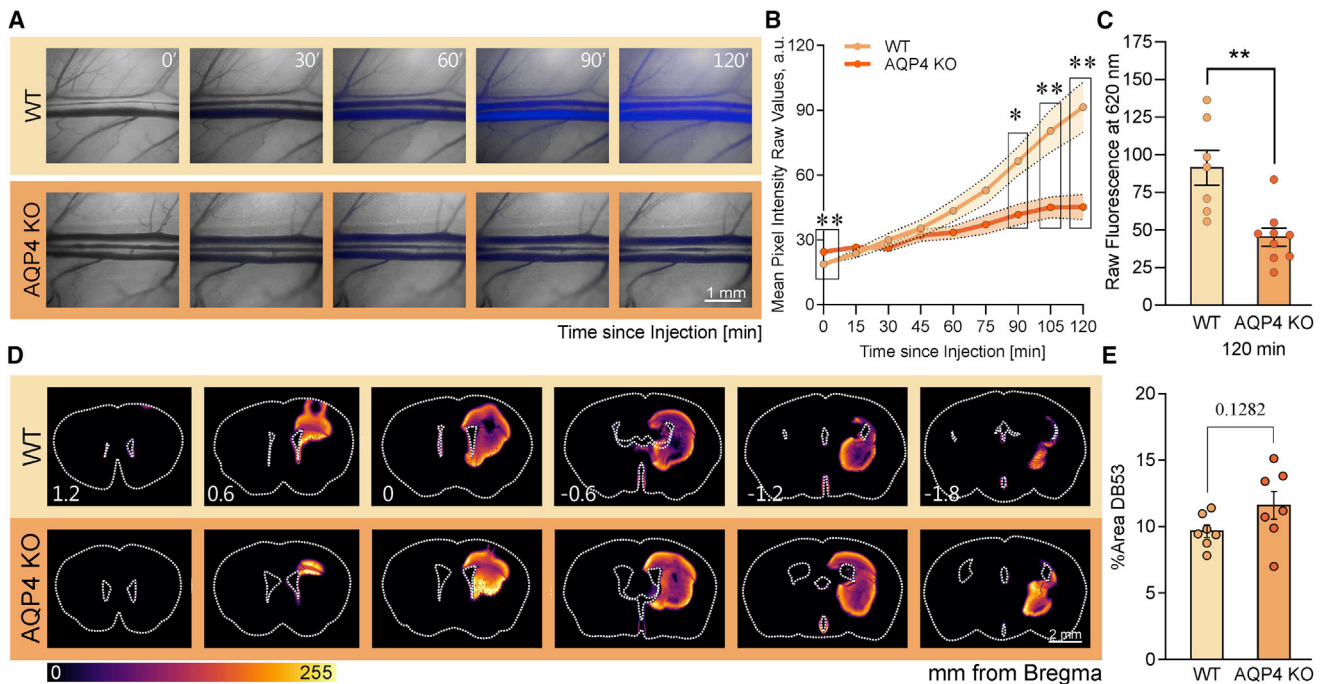


Figure 6. Clearance of DB53 is reduced in AQP4KO mice

(A) Representative *in vivo* femoral images over time for age-matched WT and AQP4KO animals.

(B) Quantification of mean pixel intensity: solid lines are mean values, shaded areas are SEM.

(C) Graph summarizing the values at the end of the assay (t = 120 min). Bars show mean and SEM, dots correspond to individual animals.

(D) Representative brain slices showing DB53 anterior/posterior distribution. Inset numbers show relative distance to bregma in millimeters.

(E) Graph showing mean percent area covered by DB53 in WT and AQP4KO animals, averaged six slices per animal, dots correspond to individual animals, error bars are SEM. *p < 0.05, **p < 0.01, ***p < 0.001, ****p < 0.0001. n ≥ 7.

DISCUSSION

DB53 has been extensively used in studies of BBB integrity because of its high affinity for binding blood albumin and long-lasting presence in plasma (Freedman and Johnson, 1969; Wolman et al., 1981; Yao et al., 2018; Yen et al., 2013). Here, we demonstrate that after intrastriate injection DB53 is freely diffusible in the parenchyma and is stable in the vascular compartment for hours. A 24 h recovery period after cannula implantation allows the glymphatic fluid transport to recover (Figures S3 and S4). EEG recordings detected no changes in neural activity during DB53 infusion, and DB53 did not aggravate reactive gliosis compared with vehicle injection (Figure S5). Interestingly, DB53 and DB53+albumin exhibited the same pattern of dispersion in the parenchyma (Figure S6), but DB53+albumin failed to clear out of the brain, pointing to the existence of an efflux barrier for larger solutes. However, it cannot be excluded that DB53 and DB53+BSA interact differently with the neuropil. Different biochemical properties of the two tracers can potentially interfere with their clearance process independently of their molecular weight. Yet, clearance of two intrastriate-delivered PEG tracers (1 and 40 kDa) (Figures 6 and 7), which are biologically inert, also exhibited size-dependent clearance kinetics. A sharp reduction of DB53 clearance was noted in AQP4KO mice (Figure 6), providing real-time *in vivo* kinetic data demonstrating that glym-

phatic clearance is dependent upon the water channel AQP4. Pharmacokinetic modeling of the data predicted that two separate efflux mechanisms coexist in healthy young adult animals (Figure 7). The DB53 clearance assay thus represents a unique quantitative *in vivo* methodology to study brain solute clearance in real time. In future studies, the assays can be used to study the effects of physiological manipulations or pathologies *in vivo*.

To our knowledge, quantitative *in vivo* data on the efflux of intraparenchymal tracers has not been collected previously. Previous studies are based on injection of fluorescent or radioactive tracers followed by quantification of the tracer remaining in the brain at different time points (Bradbury et al., 1981; Cserr et al., 1981; Yamada et al., 1991). This approach has documented a reduction of glymphatic influx in aging (Kress et al., 2014), in mice with deletion of AQP4 water channels (Iliff et al., 2012), in a murine model of Alzheimer's disease (Peng et al., 2016), and in awake compared with naturally sleeping or anesthetized (ketamine/xylazine) mice (Benveniste et al., 2017a; Xie et al., 2013). Our assay requires significantly fewer animals because the efflux kinetics of each animal is collected in real time, does not require tissue harvest thus avoiding postmortem artifacts (Ma et al., 2019; Mestre et al., 2018b), and does not require invasive blood sampling. This is a clear advantage as repeated withdrawal of blood is not feasible due to the low blood volume of mice (<2 mL in adult mice) (McGuill and Rowan, 1989). Finally,

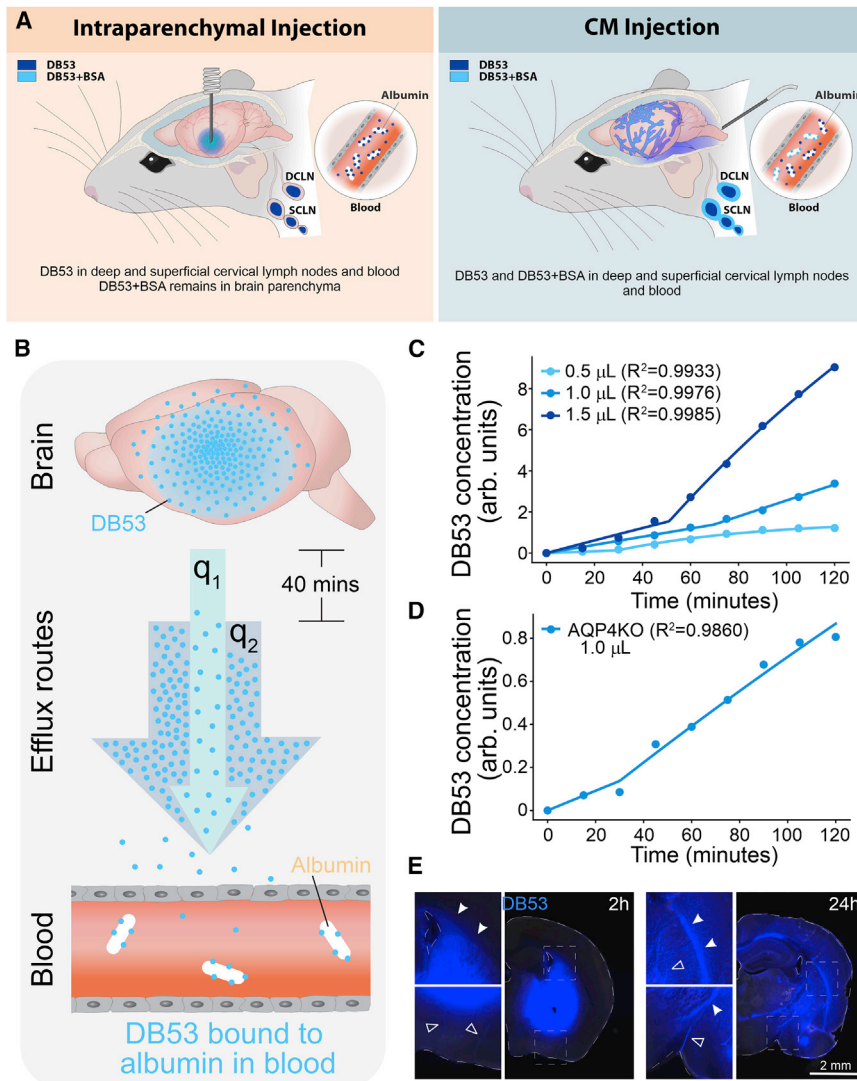


Figure 7. A two-route pharmacokinetic model is consistent with the efflux rates of DB53

(A) Graphic scheme summarizing the findings of this study.

(B) Representation of DB53 in brain (blue) being transported to blood, where it binds to albumin (white).

(C and D) Comparison of DB53 concentrations in blood after intraparenchymal injection and model estimates. Note the different scaled y axis. Dots indicate measurements, and curves show the corresponding best fits of the form specified by our pharmacokinetic model (see STAR Methods).

(E) Representative slice showing fluorescence of DB53 120 min after injection and 24 h later, with arrowheads indicating white matter tracts structures and open arrowheads pointing to major blood vessels that could increase transport rates for the second, faster efflux route. Arb. Scaled, arbitrarily scaled.

(Figure 7E, insets, and Figure S9), consistent with previous reports (Papadopoulos et al., 2005; Rosenberg et al., 1980). Perhaps the different transport mechanisms are structural: one fast through brain tissue, the other fast along fluid-facilitating structures, such as white matter tracts and major vessels. However, we cannot rule out that the differences in efflux kinetics may be influenced by downstream access to lymphatic vessels or nerve roots (Benveniste et al., 2019).

Limitations of the study

This analysis established that the kinetics of DB53 and DB53+BSA clearance is size dependent (Figures 4A–4K), a finding that was confirmed by extended the analysis to include mea-

surements of the clearance kinetics of inert PEG tracers with a molecular weight of 1 and 40 kDa (Figures 4L–4O). Although additional studies will be needed to determine whether the size limitation of clearance is a linear or a threshold function, our analysis establishes that size is a pivotal feature of glymphatic efflux. One of the most exciting future uses of the DB53 assay is to establish the importance of brain state (Han et al., 2021; Iloff et al., 2013b; Xie et al., 2013) and brain region on glymphatic clearance (Alexander et al., 2007; Maier et al., 2004; Yuan et al., 2016). Future use of the DB53 assay in pathological conditions will need to control for inflammatory environments (Amor et al., 2010; Corlier et al., 2018; Lima Giacobbo et al., 2019; Sankowski et al., 2015) and confounding factors, such as age-related changes in BBB transport (Yang et al., 2020) and autofluorescence (Burns et al., 2020; Singh Kushwaha et al., 2018). We predict that kinetic data on brain clearance obtained by the DB53 assay will aid in establishing cohesive mathematical models of brain fluid transport.

previous studies investigating the CSF efflux from the skull do not provide information on solute efflux from the brain parenchyma because ~80% of CSF (Lee et al., 2018) is shunted out of the CNS without entering the brain (Bachmann et al., 2018; Iloff et al., 2012; Kwon et al., 2017; Lee et al., 2018). In the future, mobile detection devices can be used to quantify DB53 clearance in awake mice.

Previous studies suggest that efflux of solute from the parenchyma occurs by a combination of advection and diffusion (Benveniste et al., 2019; Ray et al., 2019). Our pharmacokinetic model does not contradict advection-assisted diffusion. Our tracer is small, which always increases the relative importance of diffusion, and our assumption of well-mixed tracer distributions may well be justified exactly because bulk flow spreads the tracer. Furthermore, histological evaluation of coronal sections suggests that DB53 spreads fairly uniformly in the striatum and surrounding regions (Figures 7E and S9), but spreads more extensively along white matter tracts and blood vessels

surements of the clearance kinetics of inert PEG tracers with a molecular weight of 1 and 40 kDa (Figures 4L–4O). Although additional studies will be needed to determine whether the size limitation of clearance is a linear or a threshold function, our analysis establishes that size is a pivotal feature of glymphatic efflux. One of the most exciting future uses of the DB53 assay is to establish the importance of brain state (Han et al., 2021; Iloff et al., 2013b; Xie et al., 2013) and brain region on glymphatic clearance (Alexander et al., 2007; Maier et al., 2004; Yuan et al., 2016). Future use of the DB53 assay in pathological conditions will need to control for inflammatory environments (Amor et al., 2010; Corlier et al., 2018; Lima Giacobbo et al., 2019; Sankowski et al., 2015) and confounding factors, such as age-related changes in BBB transport (Yang et al., 2020) and autofluorescence (Burns et al., 2020; Singh Kushwaha et al., 2018). We predict that kinetic data on brain clearance obtained by the DB53 assay will aid in establishing cohesive mathematical models of brain fluid transport.

A major role of the glymphatic system is to promote clearance of brain waste, yet brain fluid and solute clearance is understudied. The observation that the rate of tracer efflux is AQP4 dependent supports the notion that AQP4 facilitates solute clearance. Controversies have surrounded the role of AQP4 in waste clearance (Mestre et al., 2020). A possible explanation for the controversies could be that the growing number of rodent (Hablitz et al., 2020; Kress et al., 2014; Peng et al., 2016; Xie et al., 2013) and human studies (Eide et al., 2021a, 2021b) have documented that waste elimination is a dynamic process dependent on the physiological state. It is thus plausible that AQP4 plays a more significant role during some physiological states than others. The DB53 clearance assay represents a much-needed tool in the studies of brain fluid transport. By implementing a simple pharmacokinetic model, we were able to provide previously unattainable insights into the kinetics of the glymphatic clearance process including multiple efflux routes from the parenchyma. Key questions that can be addressed with this methodology include the impact of neurological and systemic diseases on the brain, as well as the importance of vascular dynamics, including arterial wall pulsatility, heart rate, slow vasomotion, and the state of brain activity on the kinetics of brain waste clearance.

STAR★METHODS

Detailed methods are provided in the online version of this paper and include the following:

- KEY RESOURCES TABLE
- RESOURCE AVAILABILITY
 - Lead contact
 - Materials availability
 - Data and code availability
- EXPERIMENTAL MODEL AND SUBJECT DETAILS
- METHOD DETAILS
 - Drugs
 - Fluorescent tracers
 - Intravenous injections
 - Intracerebral cannula implant
 - Intra-striatal acute tracer injections
 - Clearance assay
 - Cisterna magna (CM) tracer injections
 - *In vivo* lymph node imaging
 - Intra-striatal PEG tracer co-injections
 - Immunohistochemistry
 - Electroencephalogram recordings
 - Size-selectivity efflux assessment
 - Formamide extraction
 - Intracranial pressure (ICP) measurements
 - Quantitative image analysis
 - Mathematical model
- QUANTIFICATION AND STATISTICAL ANALYSIS

SUPPLEMENTAL INFORMATION

Supplemental information can be found online at <https://doi.org/10.1016/j.celrep.2022.111320>.

ACKNOWLEDGMENTS

We thank Dan Xue for expert graphical support. This project has received funding from the Dr. Miriam and Sheldon G. Adelson Medical Research Foundation, the NIH/NINDS/NIA (R01NS100366, RF1AG057575), the Novo Nordisk and the Lundbeck Foundation, as well as by the US Army Research Office (grant MURI W911NF1910280). The views and conclusions contained in this review are solely those of the authors and should not be interpreted as representing the policies, either expressed or implied, of the sponsors, the National Institutes of Health, the Army Research Office, or the US Government. The US Government is authorized to reproduce and distribute reprints for Government purposes notwithstanding any copyright notation herein.

AUTHOR CONTRIBUTIONS

V.P. and M.N. conceived the experimental design. V.P., G.O., A.H., A.L.-d.-G., M.J.G., and L.M.H. provided data collection. V.P., G.O., A.H., and A.L.-d.-G. performed data analysis. V.P. carried out figure preparation. P.B. and D.H.K. carried out pharmacokinetic modeling. V.P., L.M.H., and M.N. contributed to manuscript writing and preparation. R.H. and W.W. provided resources and unpublished data. All authors read and approved the final version of this manuscript.

DECLARATION OF INTERESTS

The authors declare no competing interests.

Received: June 10, 2021

Revised: February 5, 2022

Accepted: August 16, 2022

Published: September 13, 2022

REFERENCES

- Abbott, N.J., Pizzo, M.E., Preston, J.E., Janigro, D., and Thorne, R.G. (2018). The role of brain barriers in fluid movement in the CNS: is there a 'glymphatic' system? *Acta Neuropathol.* 135, 387–407. <https://doi.org/10.1007/s00401-018-1812-4>.
- Alexander, A.L., Lee, J.E., Lazar, M., and Field, A.S. (2007). Diffusion tensor imaging of the brain. *Neurotherapeutics* 4, 316–329. <https://doi.org/10.1016/j.nurt.2007.05.011>.
- Amor, S., Puentes, F., Baker, D., and van der Valk, P. (2010). Inflammation in neurodegenerative diseases. *Immunology* 129, 154–169. <https://doi.org/10.1111/j.1365-2567.2009.03225.x>.
- Bachmann, S.B., Detmar, M., and Proulx, S.T. (2018). Visualization and measurement of lymphatic function in vivo. *Methods Mol. Biol.* 1846, 197–211. https://doi.org/10.1007/978-1-4939-8712-2_13.
- Bedussi, B., van Lier, M.G.J.T.B., Bartstra, J.W., de Vos, J., Siebes, M., Van-Bavel, E., and Bakker, E.N.T.P. (2015). Clearance from the mouse brain by convection of interstitial fluid towards the ventricular system. *Fluids Barriers CNS* 12, 23. <https://doi.org/10.1186/s12987-015-0019-5>.
- Benveniste, H., and Diemer, N.H. (1987). Cellular reactions to implantation of a microdialysis tube in the rat hippocampus. *Acta Neuropathol.* 74, 234–238. <https://doi.org/10.1007/BF00688186>.
- Benveniste, H., Lee, H., Ding, F., Sun, Q., Al-Bizri, E., Makaryus, R., Probst, S., Nedergaard, M., Stein, E.A., and Lu, H. (2017a). Anesthesia with dexmedetomidine and low-dose isoflurane increases solute transport via the glymphatic pathway in rat brain when compared with high-dose isoflurane. *Anesthesiology* 127, 976–988. <https://doi.org/10.1097/ALN.0000000000001888>.
- Benveniste, H., Lee, H., and Volkow, N.D. (2017b). The glymphatic pathway: waste removal from the CNS via cerebrospinal fluid transport. *Neuroscientist* 23, 454–465. <https://doi.org/10.1177/1073858417691030>.
- Benveniste, H., Liu, X., Koundal, S., Sanggaard, S., Lee, H., and Wardlaw, J. (2019). The glymphatic system and waste clearance with brain aging: a review. *Gerontology* 65, 106–119. <https://doi.org/10.1159/000490349>.

- Binder, D.K., Papadopoulos, M.C., Haggie, P.M., and Verkman, A.S. (2004). In vivo measurement of brain extracellular space diffusion by cortical surface photobleaching. *J. Neurosci.* *24*, 8049–8056. <https://doi.org/10.1523/JNEUROSCI.2294-04.2004>.
- Bradbury, M.W., Cserr, H.F., and Westrop, R.J. (1981). Drainage of cerebral interstitial fluid into deep cervical lymph of the rabbit. *Am. J. Phys.* *240*, F329–F336. <https://doi.org/10.1152/ajprenal.1981.240.4.F329>.
- Brady, C.E., 3rd, DiPalma, J.A., Morawski, S.G., Santa Ana, C.A., and Fordtran, J.S. (1986). Urinary excretion of polyethylene glycol 3350 and sulfate after gut lavage with a polyethylene glycol electrolyte lavage solution. *Gastroenterology* *90*, 1914–1918. [https://doi.org/10.1016/0016-5085\(86\)90261-1](https://doi.org/10.1016/0016-5085(86)90261-1).
- Burns, J.C., Cotleur, B., Walther, D.M., Bajrami, B., Rubino, S.J., Wei, R., Franchimont, N., Cotman, S.L., Ransohoff, R.M., and Mingueneau, M. (2020). Differential accumulation of storage bodies with aging defines discrete subsets of microglia in the healthy brain. *Elife* *9*, e57495. <https://doi.org/10.7554/eLife.57495>.
- Clement, C.C., Wang, W., Dzieciatkowska, M., Cortese, M., Hansen, K.C., Becerra, A., Thangaswamy, S., Nizamutdinova, I., Moon, J.-Y., Stern, L.J., et al. (2018). Quantitative profiling of the lymph node clearance capacity. *Sci. Rep.* *8*, 11253. <https://doi.org/10.1038/s41598-018-29614-0>.
- Connolly, D.C., and Wood, E.H. (1954). Simultaneous measurement of the appearance and disappearance of T-1824 (Evans blue) in blood and tissue after intravenous injection in man. *J. Appl. Physiol.* *7*, 73–83. <https://doi.org/10.1152/jappl.1954.7.1.73>.
- Cortier, F., Hafzalla, G., Faskowitz, J., Kuller, L.H., Becker, J.T., Lopez, O.L., Thompson, P.M., and Braskie, M.N. (2018). Systemic inflammation as a predictor of brain aging: contributions of physical activity, metabolic risk, and genetic risk. *Neuroimage* *172*, 118–129. <https://doi.org/10.1016/j.neuroimage.2017.12.027>.
- Cserr, H.F., Cooper, D.N., Suri, P.K., and Patlak, C.S. (1981). Efflux of radiolabeled polyethylene glycols and albumin from rat brain. *Am. J. Physiol.* *240*, F319–F328. <https://doi.org/10.1152/ajprenal.1981.240.4.F319>.
- Davoodi-Bojd, E., Ding, G., Zhang, L., Li, Q., Li, L., Chopp, M., Zhang, Z., and Jiang, Q. (2019). Modeling glymphatic system of the brain using MRI. *Neuroimage* *188*, 616–627. <https://doi.org/10.1016/j.neuroimage.2018.12.039>.
- Dawson, A.B., Evans, H.M., and Whipple, G.H. (1920). Blood volume studies. *Am. J. Physiol-Leg. Content* *57*, 232–256. <https://doi.org/10.1152/ajplegacy.1920.51.2.232>.
- Eide, P.K., Mariussen, E., Uggerud, H., Pripp, A.H., Lashkarivand, A., Hassel, B., Christensen, H., Hovd, M.H., and Ringstad, G. (2021a). Clinical application of intrathecal gadobutrol for assessment of cerebrospinal fluid tracer clearance to blood. *JCI Insight* *6*, 147063. <https://doi.org/10.1172/jci.insight.147063>.
- Eide, P.K., Vinje, V., Pripp, A.H., Mardal, K.A., and Ringstad, G. (2021b). Sleep deprivation impairs molecular clearance from the human brain. *Brain* *144*, 863–874. <https://doi.org/10.1093/brain/awaa443>.
- Evans, H.M., and Schulemann, W. (1914). The action of vital stains belonging to the benzidine group. *Science* *39*, 443–454. <https://doi.org/10.1126/science.39.1004.443>.
- Freedman, F.B., and Johnson, J.A. (1969). Equilibrium and kinetic properties of the Evans blue-albumin system. *Am. J. Physiol.* *216*, 675–681. <https://doi.org/10.1152/ajplegacy.1969.216.3.675>.
- Giannetto, M., Xia, M., Stæger, F.F., Metcalfe, T., Vinitzky, H.S., Dang, J.A.M.L., Xavier, A.L.R., Kress, B.T., Nedergaard, M., and Hablitz, L.M. (2020). Biological sex does not predict glymphatic influx in healthy young, middle aged or old mice. *Sci. Rep.* *10*, 16073. <https://doi.org/10.1038/s41598-020-72621-3>.
- Giger, M., Baumgartner, H.R., and Zbinden, G. (1974). Toxicological effects of Evans blue and Congo red on blood platelets. *Agents Actions* *4*, 173–180. <https://doi.org/10.1007/bf01970259>.
- Graesser, D., Solowiej, A., Bruckner, M., Osterweil, E., Juedes, A., Davis, S., Ruddle, N.H., Engelhardt, B., and Madri, J.A. (2002). Altered vascular permeability and early onset of experimental autoimmune encephalomyelitis in PECAM-1-deficient mice. *J. Clin. Invest.* *109*, 383–392. <https://doi.org/10.1172/jci13595>.
- Groothuis, D.R., Vavra, M.W., Schlageter, K.E., Kang, E.W.Y., Itskovich, A.C., Hertzler, S., Allen, C.V., and Lipton, H.L. (2007). Efflux of drugs and solutes from brain: the interactive roles of diffusional transcapillary transport, bulk flow and capillary transporters. *J. Cereb. Blood Flow Metab.* *27*, 43–56. <https://doi.org/10.1038/sj.jcbfm.9600315>.
- Hablitz, L.M., Plá, V., Giannetto, M., Vinitzky, H.S., Stæger, F.F., Metcalfe, T., Nguyen, R., Benrais, A., and Nedergaard, M. (2020). Circadian control of brain glymphatic and lymphatic fluid flow. *Nat. Commun.* *11*, 4411. <https://doi.org/10.1038/s41467-020-18115-2>.
- Hablitz, L.M., Vinitzky, H.S., Sun, Q., Stæger, F.F., Sigurdsson, B., Mortensen, K.N., Lilius, T.O., and Nedergaard, M. (2019). Increased glymphatic influx is correlated with high EEG delta power and low heart rate in mice under anesthesia. *Sci. Adv.* *5*, eaav5447. <https://doi.org/10.1126/sciadv.aav5447>.
- Hamidi, M., Azadi, A., and Rafiei, P. (2006). Pharmacokinetic consequences of pegylation. *Drug Deliv.* *13*, 399–409. <https://doi.org/10.1080/10717540600814402>.
- Han, F., Chen, J., Belkin-Rosen, A., Gu, Y., Luo, L., Buxton, O.M., and Liu, X.; Alzheimer's Disease Neuroimaging Initiative (2021). Reduced coupling between cerebrospinal fluid flow and global brain activity is linked to Alzheimer disease-related pathology. *PLoS Biol.* *19*, e3001233. <https://doi.org/10.1371/journal.pbio.3001233>.
- Hladky, S.B., and Barrand, M.A. (2014). Mechanisms of fluid movement into, through and out of the brain: evaluation of the evidence. *Fluids Barriers CNS* *11*, 26. <https://doi.org/10.1186/2045-8118-11-26>.
- Iliff, J.J., Chen, M.J., Plog, B.A., Zeppenfeld, D.M., Soltero, M., Yang, L., Singh, I., Deane, R., and Nedergaard, M. (2014). Impairment of glymphatic pathway function promotes tau pathology after traumatic brain injury. *J. Neurosci.* *34*, 16180–16193. <https://doi.org/10.1523/JNEUROSCI.3020-14.2014>.
- Iliff, J.J., Lee, H., Yu, M., Feng, T., Logan, J., Nedergaard, M., and Benveniste, H. (2013a). Brain-wide pathway for waste clearance captured by contrast-enhanced MRI. *J. Clin. Invest.* *123*, 1299–1309. <https://doi.org/10.1172/JCI67677>.
- Iliff, J.J., and Nedergaard, M. (2013). Is there a cerebral lymphatic system? *Stroke* *44*, S93–S95. <https://doi.org/10.1161/STROKEAHA.112.678698>.
- Iliff, J.J., Wang, M., Liao, Y., Plogg, B.A., Peng, W., Gundersen, G.A., Benveniste, H., Vates, G.E., Deane, R., Goldman, S.A., et al. (2012). A paravascular pathway facilitates CSF flow through the brain parenchyma and the clearance of interstitial solutes, including amyloid beta. *Sci. Transl. Med.* *4*, 147ra111. <https://doi.org/10.1126/scitranslmed.3003748>.
- Iliff, J.J., Wang, M., Zeppenfeld, D.M., Venkataraman, A., Plog, B.A., Liao, Y., Deane, R., and Nedergaard, M. (2013b). Cerebral arterial pulsation drives paravascular CSF–interstitial fluid exchange in the murine brain. *J. Neurosci.* *33*, 18190–18199. <https://doi.org/10.1523/jneurosci.1592-13.2013>.
- Katayama, S., Shionoya, H., and Ohtake, S. (1978). A new method for extraction of extravasated dye in the skin and the influence of fasting stress on passive cutaneous anaphylaxis in Guinea pigs and rats. *Microbiol. Immunol.* *22*, 89–101. <https://doi.org/10.1111/j.1348-0421.1978.tb00352.x>.
- Kiviniemi, V., Wang, X., Korhonen, V., Keinänen, T., Tuovinen, T., Autio, J., LeVan, P., Keilholz, S., Zang, Y.F., Hennig, J., and Nedergaard, M. (2016). Ultrafast magnetic resonance encephalography of physiological brain activity – glymphatic pulsation mechanisms? *J. Cereb. Blood Flow Metab.* *36*, 1033–1045. <https://doi.org/10.1177/0271678x15622047>.
- Kozai, T.D.Y., Jaquins-Gerstl, A.S., Vazquez, A.L., Michael, A.C., and Cui, X.T. (2015). Brain tissue responses to neural implants impact signal sensitivity and intervention strategies. *ACS Chem. Neurosci.* *6*, 48–67. <https://doi.org/10.1021/cn500256e>.
- Kress, B.T., Iliff, J.J., Xia, M., Wang, M., Wei, H.S., Zeppenfeld, D., Xie, L., Kang, H., Xu, Q., Liew, J.A., et al. (2014). Impairment of paravascular clearance pathways in the aging brain. *Ann. Neurol.* *76*, 845–861. <https://doi.org/10.1002/ana.24271>.

- Kwon, S., Janssen, C.F., Velasquez, F.C., and Sevcik-Muraca, E.M. (2017). Fluorescence imaging of lymphatic outflow of cerebrospinal fluid in mice. *J. Immunol. Methods* 449, 37–43. <https://doi.org/10.1016/j.jim.2017.06.010>.
- Lee, H., Mortensen, K., Sanggaard, S., Koch, P., Brunner, H., Quistorff, B., Nedergaard, M., and Benveniste, H. (2018). Quantitative Gd-DOTA uptake from cerebrospinal fluid into rat brain using 3D VFA-SPGR at 9.4T. *Magn. Reson. Med.* 79, 1568–1578. <https://doi.org/10.1002/mrm.26779>.
- Lee, H., Xie, L., Yu, M., Kang, H., Feng, T., Deane, R., Logan, J., Nedergaard, M., and Benveniste, H. (2015). The effect of body posture on brain glymphatic transport. *J. Neurosci.* 35, 11034–11044. <https://doi.org/10.1523/JNEUROSCI.1625-15.2015>.
- Lima Giacobbo, B., Doorduyn, J., Klein, H.C., Dierckx, R.A.J.O., Bromberg, E., and de Vries, E.F.J. (2019). Brain-derived neurotrophic factor in brain disorders: focus on Neuroinflammation. *Mol. Neurobiol.* 56, 3295–3312. <https://doi.org/10.1007/s12035-018-1283-6>.
- Lundgaard, I., Lu, M.L., Yang, E., Peng, W., Mestre, H., Hitomi, E., Deane, R., and Nedergaard, M. (2017). Glymphatic clearance controls state-dependent changes in brain lactate concentration. *J. Cereb. Blood Flow Metab.* 37, 2112–2124. <https://doi.org/10.1177/0271678x16661202>.
- Ma, Q., Ries, M., Decker, Y., Müller, A., Riner, C., Bücker, A., Fassbender, K., Detmar, M., and Proulx, S.T. (2019). Rapid lymphatic efflux limits cerebrospinal fluid flow to the brain. *Acta Neuropathol.* 137, 151–165. <https://doi.org/10.1007/s00401-018-1916-x>.
- Maier, S.E., Vajapeyam, S., Mamata, H., Westin, C.F., Jolesz, F.A., and Mukherjee, R.V. (2004). Biexponential diffusion tensor analysis of human brain diffusion data. *Magn. Reson. Med.* 51, 321–330. <https://doi.org/10.1002/mrm.10685>.
- Manaenko, A., Chen, H., Kammer, J., Zhang, J.H., and Tang, J. (2011). Comparison Evans Blue injection routes: intravenous versus intraperitoneal, for measurement of blood-brain barrier in a mice hemorrhage model. *J. Neurosci. Methods* 195, 206–210. <https://doi.org/10.1016/j.jneumeth.2010.12.013>.
- McGuill, M.W., and Rowan, A.N. (1989). Biological effects of blood loss: implications for sampling volumes and techniques. *ILAR J.* 31, 5–20. <https://doi.org/10.1093/ilar.31.4.5>.
- Mestre, H., Hablitz, L.M., Xavier, A.L., Feng, W., Zou, W., Pu, T., Monai, H., Murlidharan, G., Castellanos Rivera, R.M., Simon, M.J., et al. (2018a). Aquaporin-4-dependent glymphatic solute transport in the rodent brain. *Elife* 7, e40070. <https://doi.org/10.7554/eLife.40070>.
- Mestre, H., Mori, Y., and Nedergaard, M. (2020). The brain's glymphatic system: current controversies. *Trends Neurosci.* 43, 458–466. <https://doi.org/10.1016/j.tins.2020.04.003>.
- Mestre, H., Tithof, J., Du, T., Song, W., Peng, W., Sweeney, A.M., Olveda, G., Thomas, J.H., Nedergaard, M., and Kelley, D.H. (2018b). Flow of cerebrospinal fluid is driven by arterial pulsations and is reduced in hypertension. *Nat. Commun.* 9, 4878. <https://doi.org/10.1038/s41467-018-07318-3>.
- Miller, W.G., and Inker, L.A. (2020). Chapter 35 - laboratory evaluation of kidney function. In *Contemporary Practice in Clinical Chemistry*, Fourth Edition, W. Clarke and M.A. Marzinko, eds. (Academic Press), pp. 611–628. <https://doi.org/10.1016/B978-0-12-815499-1.00035-1>.
- Murlidharan, G., Crowther, A., Reardon, R.A., Song, J., and Asokan, A. (2016). Glymphatic fluid transport controls paravascular clearance of AAV vectors from the brain. *JCI Insight* 1, e88034. <https://doi.org/10.1172/jci.insight.88034>.
- Naessens, D.M.P., Dobbe, J.G.G., de Vos, J., VanBavel, E., and Bakker, E.N.T.P. (2021). Mapping solute clearance from the mouse Hippocampus using a 3D imaging cryomicrotome. *Front. Neurosci.* 15, 631325. <https://doi.org/10.3389/fnins.2021.631325>.
- Nicholson, C., and Syková, E. (1998). Extracellular space structure revealed by diffusion analysis. *Trends Neurosci.* 21, 207–215. [https://doi.org/10.1016/S0166-2236\(98\)01261-2](https://doi.org/10.1016/S0166-2236(98)01261-2).
- Nicholson, C., and Tao, L. (1993). Hindered diffusion of high molecular weight compounds in brain extracellular microenvironment measured with integrative optical imaging. *Biophys. J.* 65, 2277–2290. [https://doi.org/10.1016/S0006-3495\(93\)81324-9](https://doi.org/10.1016/S0006-3495(93)81324-9).
- Papadopoulos, M.C., Kim, J.K., and Verkman, A.S. (2005). Extracellular space diffusion in central nervous system: anisotropic diffusion measured by elliptical surface photobleaching. *Biophys. J.* 89, 3660–3668. <https://doi.org/10.1529/biophysj.105.068114>.
- Pelham, R.W., Nix, L.C., Chavira, R.E., Cleveland, M.V., and Stetson, P. (2008). Clinical trial: single- and multiple-dose pharmacokinetics of polyethylene glycol (PEG-3350) in healthy young and elderly subjects. *Aliment. Pharmacol. Ther.* 28, 256–265. <https://doi.org/10.1111/j.1365-2036.2008.03727.x>.
- Peng, W., Acharyar, T.M., Li, B., Liao, Y., Mestre, H., Hitomi, E., Regan, S., Kasper, T., Peng, S., Ding, F., et al. (2016). Suppression of glymphatic fluid transport in a mouse model of Alzheimer's disease. *Neurobiol. Dis.* 93, 215–225. <https://doi.org/10.1016/j.nbd.2016.05.015>.
- Rabinowitz, J.D., and Enerbäck, S. (2020). Lactate: the ugly duckling of energy metabolism. *Nat. Metab.* 2, 566–571. <https://doi.org/10.1038/s42255-020-0243-4>.
- Radu, M., and Chernoff, J. (2013). An in vivo assay to test blood vessel permeability. *J. Vis. Exp.*, e50062. <https://doi.org/10.3791/50062>.
- Rasmussen, M.K., Mestre, H., and Nedergaard, M. (2021). Fluid transport in the brain. *Physiol. Rev.* 102, 1025–1151. <https://doi.org/10.1152/physrev.00031.2020>.
- Ray, L., Iliff, J.J., and Heys, J.J. (2019). Analysis of convective and diffusive transport in the brain interstitium. *Fluids Barriers CNS* 16, 6. <https://doi.org/10.1186/s12987-019-0126-9>.
- Reeve, E.B. (1957). The contribution of I 131-labeled proteins to measurements of blood volume. *Ann. N. Y. Acad. Sci.* 70, 137–147. <https://doi.org/10.1111/j.1749-6632.1957.tb35384.x>.
- Rennels, M.L., Blaumanis, O.R., and Grady, P.A. (1990). Rapid solute transport throughout the brain via paravascular fluid pathways. *Adv. Neurol.* 52, 431–439.
- Rennels, M.L., Gregory, T.F., Blaumanis, O.R., Fujimoto, K., and Grady, P.A. (1985). Evidence for a 'paravascular' fluid circulation in the mammalian central nervous system, provided by the rapid distribution of tracer protein throughout the brain from the subarachnoid space. *Brain Res.* 326, 47–63. [https://doi.org/10.1016/0006-8993\(85\)91383-6](https://doi.org/10.1016/0006-8993(85)91383-6).
- Ringstad, G., Valnes, L.M., Dale, A.M., Pripp, A.H., Vatnehol, S.A.S., Emblem, K.E., Mardal, K.A., and Eide, P.K. (2018). Brain-wide glymphatic enhancement and clearance in humans assessed with MRI. *JCI Insight* 3, 121537. <https://doi.org/10.1172/jci.insight.121537>.
- Ringstad, G., Vatnehol, S.A.S., and Eide, P.K. (2017). Glymphatic MRI in idiopathic normal pressure hydrocephalus. *Brain* 140, 2691–2705. <https://doi.org/10.1093/brain/awx191>.
- Roberts, M.J., Bentley, M.D., and Harris, J.M. (2002). Chemistry for peptide and protein PEGylation. *Adv. Drug Deliv. Rev.* 54, 459–476. [https://doi.org/10.1016/S0169-409X\(02\)00022-4](https://doi.org/10.1016/S0169-409X(02)00022-4).
- Roselli, R.J., and Diller, K.R. (2011). *Biotransport: Principles and Applications* (Springer Science+Business Media, LLC).
- Rosenberg, G.A., Kyner, W.T., and Estrada, E. (1980). Bulk flow of brain interstitial fluid under normal and hyperosmolar conditions. *Am. J. Physiol.* 238, F42–F49. <https://doi.org/10.1152/ajprenal.1980.238.1.F42>.
- Rusakov, D.A., and Kullmann, D.M. (1998). A tortuous and viscous route to understanding diffusion in the brain. *Trends Neurosci.* 21, 469–470. [https://doi.org/10.1016/S0166-2236\(98\)01309-5](https://doi.org/10.1016/S0166-2236(98)01309-5).
- Sankowski, R., Mader, S., and Valdés-Ferrer, S.I. (2015). Systemic inflammation and the brain: novel roles of genetic, molecular, and environmental cues as drivers of neurodegeneration. *Front. Cell. Neurosci.* 9, 28. <https://doi.org/10.3389/fncel.2015.00028>.
- Saria, A., and Lundberg, J.M. (1983). Evans blue fluorescence: quantitative and morphological evaluation of vascular permeability in animal tissues. *J. Neurosci. Methods* 8, 41–49. [https://doi.org/10.1016/0165-0270\(83\)90050-x](https://doi.org/10.1016/0165-0270(83)90050-x).

- Saunders, N.R., Dreifuss, J.J., Dziegielewska, K.M., Johansson, P.A., Habgood, M.D., Møllgård, K., and Bauer, H.C. (2014). The rights and wrongs of blood-brain barrier permeability studies: a walk through 100 years of history. *Front. Neurosci.* 8, 404. <https://doi.org/10.3389/fnins.2014.00404>.
- Saunders, N.R., Dziegielewska, K.M., Møllgård, K., and Habgood, M.D. (2015). Markers for blood-brain barrier integrity: how appropriate is Evans blue in the twenty-first century and what are the alternatives? *Front. Neurosci.* 9, 385. <https://doi.org/10.3389/fnins.2015.00385>.
- Simmons, J.M., Lee, Y.W., and Achenie, L. (2018). A passive diffusion model of fluorescein derivatives in an in vitro human brain microvascular endothelial cell (HBMEC) monolayer. *Journal of Measurements in Engineering* 6, 127–136. <https://doi.org/10.21595/jme.2018.20186>.
- Singh Kushwaha, S., Patro, N., and Kumar Patro, I. (2018). A sequential study of age-related lipofuscin accumulation in Hippocampus and striate cortex of rats. *Ann. Neurosci.* 25, 223–233. <https://doi.org/10.1159/000490908>.
- Spector, R., Robert Snodgrass, S., and Johanson, C.E. (2015). A balanced view of the cerebrospinal fluid composition and functions: focus on adult humans. *Exp. Neurol.* 273, 57–68. <https://doi.org/10.1016/j.expneurol.2015.07.027>.
- Steinwall, O., and Klatzo, I. (1966). Selective vulnerability of the blood-brain barrier in chemically induced lesions. *J. Neuropathol. Exp. Neurol.* 25, 542–559. <https://doi.org/10.1097/00005072-196610000-00004>.
- Syková, E., and Nicholson, C. (2008). Diffusion in brain extracellular space. *Physiol. Rev.* 88, 1277–1340. <https://doi.org/10.1152/physrev.00027.2007>.
- Thrane, A.S., Rappold, P.M., Fujita, T., Torres, A., Bekar, L.K., Takano, T., Peng, W., Wang, F., Rangroo Thrane, V., Enger, R., et al. (2011). Critical role of aquaporin-4 (AQP4) in astrocytic Ca²⁺ signaling events elicited by cerebral edema. *Proc. Natl. Acad. Sci. USA* 108, 846–851. <https://doi.org/10.1073/pnas.1015217108>.
- Vilstrup, H. (1980). Synthesis of urea after stimulation with amino acids: relation to liver function. *Gut* 21, 990–995. <https://doi.org/10.1136/gut.21.11.990>.
- Virtanen, P., Gommers, R., Oliphant, T.E., Haberland, M., Reddy, T., Cournapeau, D., Burovski, E., Peterson, P., Weckesser, W., Bright, J., et al. (2020). SciPy 1.0: fundamental algorithms for scientific computing in Python. *Nat. Methods* 17, 261–272. <https://doi.org/10.1038/s41592-019-0686-2>.
- Wellman, S.M., and Kozai, T.D.Y. (2017). Understanding the inflammatory tissue reaction to brain implants to improve Neurochemical sensing performance. *ACS Chem. Neurosci.* 8, 2578–2582. <https://doi.org/10.1021/acchemneuro.7b00403>.
- Wolman, M., Klatzo, I., Chui, E., Wilmes, F., Nishimoto, K., Fujiwara, K., and Spatz, M. (1981). Evaluation of the dye-protein tracers in pathophysiology of the blood-brain barrier. *Acta Neuropathol.* 54, 55–61. <https://doi.org/10.1007/bf00691332>.
- Xavier, A.L.R., Hauglund, N.L., von Holstein-Rathlou, S., Li, Q., Sanggaard, S., Lou, N., Lundgaard, I., and Nedergaard, M. (2018). Cannula implantation into the cisterna magna of rodents. *J Vis Exp.* <https://doi.org/10.3791/57378>.
- Xie, L., Kang, H., Xu, Q., Chen, M.J., Liao, Y., Thiyagarajan, M., O'Donnell, J., Christensen, D.J., Nicholson, C., Iliff, J.J., et al. (2013). Sleep drives metabolite clearance from the adult brain. *Science* 342, 373–377. <https://doi.org/10.1126/science.1241224>.
- Yamada, S., DePasquale, M., Patlak, C.S., and Cserr, H.F. (1991). Albumin outflow into deep cervical lymph from different regions of rabbit brain. *Am. J. Physiol.* 261, H1197–H1204. <https://doi.org/10.1152/ajpheart.1991.261.4.H1197>.
- Yang, A.C., Stevens, M.Y., Chen, M.B., Lee, D.P., Stähli, D., Gate, D., Contrepois, K., Chen, W., Iram, T., Zhang, L., et al. (2020). Physiological blood-brain transport is impaired with age by a shift in transcytosis. *Nature* 583, 425–430. <https://doi.org/10.1038/s41586-020-2453-z>.
- Yao, L., Xue, X., Yu, P., Ni, Y., and Chen, F. (2018). Evans blue dye: a revisit of its applications in biomedicine. *Contrast Media Mol. Imaging* 2018, 7628037. <https://doi.org/10.1155/2018/7628037>.
- Yen, L.F., Wei, V.C., Kuo, E.Y., and Lai, T.W. (2013). Distinct patterns of cerebral extravasation by Evans blue and sodium fluorescein in rats. *PLoS One* 8, e68595. <https://doi.org/10.1371/journal.pone.0068595>.
- Yuan, L., Sun, M., Chen, Y., Long, M., Zhao, X., Yin, J., Yan, X., Ji, D., and Ni, H. (2016). Non-Gaussian diffusion alterations on diffusion kurtosis imaging in patients with early Alzheimer's disease. *Neurosci. Lett.* 616, 11–18. <https://doi.org/10.1016/j.neulet.2016.01.021>.

STAR★METHODS

KEY RESOURCES TABLE

REAGENT or RESOURCE	SOURCE	IDENTIFIER
Antibodies		
Anti-Glial Fibrillary Acidic Protein Antibody, clone GA5	Millipore	MAB360;RRID: AB_11212597
Anti-Iba1 antibody	Abcam	ab5076; RRID: AB_2224402
Cy TM 3 AffiniPure Donkey Anti-Mouse IgG	Jackson ImmunoResearch	715165151; RRID: AB_2315777
Cy TM 3 AffiniPure Donkey Anti-Goat IgG	Jackson ImmunoResearch	705165147; RRID: AB_2307351
Chemicals, peptides, and recombinant proteins		
10kDa-Dextran-FITC emerald	Thermo Scientific	D1820
Direct blue 53	Sigma-Aldrich	E2129
Isotonic saline solution	Ricca Chemical Company	R7210000
Fluorescein	Sigma-Aldrich	F2456
FITC-PEG 1 kDa	Creative PEGWorks	PSB-2256
Rhodamine-PEG 40 kDa	Creative PEGWorks	PSB-2260
BSA	Millipore Sigma	A8806
Formamide	Sigma-Aldrich	11814320001
Experimental models: Organisms/strains		
C57BL/6 mice	Charles River Laboratories	C57BL/6NCRl
AQP4 <i>knockout</i> and wildtype littermate mice on a C57BL/6 background	University of Rochester Vivarium	AQP4KO/WT
Software and algorithms		
MATLAB	MathWorks	R2020
AxoScope software	Axon Instruments	pCLAMP 11.1
ImageJ software	NIH	Version 1.53q
GraphPad Prism	Dotmatics	Version 8
Other		
Guide cannula 26G	PlasticsOne	C315G SPC
Inner infusion cannula 33G	PlasticsOne	C315I/SP
Dummy Cannula 33G	PlasticsOne	C315DC/SP
50 kDa cutoff Amicon Ultra-0.5 Centrifugal Filter Unit	Millipore Sigma	UFC505024
24G i.v. catheter Surflo®	Terumo, Somerset	SR-OX2419CA
1 mL syringe	Becton& Dickinson	309650
EDTA-tubes MiniCollect®	Greiner Bio-One	450474

RESOURCE AVAILABILITY

Lead contact

Further information and requests for resources should be directed to and will be fulfilled by the lead contact, Maiken Nedergaard (maiken_nedergaard@urmc.rochester.edu).

Materials availability

This study did not generate new unique reagents.

Data and code availability

- All data reported in this paper will be shared by the [lead contact](#) upon request.
- This paper does not report original code.
- Any additional information required to reanalyze the data reported in this paper is available from the [lead contact](#) upon request.

EXPERIMENTAL MODEL AND SUBJECT DETAILS

Male, C57BL/6 mice (2.5 ± 0.4 months old) purchased from Charles River Laboratories (Wilmington, MA, USA) were used for all experiments unless otherwise specified. For assessing the effect of AQP4 water channel on glymphatic clearance, AQP4 *knockout* (AQP4KO) and WT littermate mice on a C57BL/6 background (Mestre et al., 2018a; Thrane et al., 2011) bred in the University of Rochester Vivarium were used. We found no significant differences between sexes in glymphatic influx or glymphatic clearance (data not shown), consistent with previous results (Giannetto et al., 2020). Further details on age and weight of the used animals can be found in Table S1. Mice were group-housed in a 12h light/12h dark cycle with *ad libitum* access to food and water. All experiments were performed in the light phase. Animal husbandry and experimental procedures involving animal subjects were approved by the University of Rochester Medical Center Committee on Animal Resources. All efforts were made to keep animal usage to a minimum.

METHOD DETAILS

Drugs

Anesthesia was administered as follows: a mixture of racemic ketamine (100 mg/kg) and xylazine (20 mg/kg) intraperitoneally (IP). For poly(ethylene glycol) (PEG) clearance, isoflurane was used with an initial induction at 4%, maintained at 1% to 2% in oxygen for the duration of the infusion. Depth of anesthesia was determined by the pedal reflex test. If the mouse responded to toe pinch an additional 1/10 of the initial dosage was given and the tracer experiment was delayed until full unconsciousness was obtained. Pedal reflex was tested every 10 min during the experiment to ensure proper anesthesia throughout the study. A 37°C temperature-controlled pad was used to maintain body temperature on animals under anesthesia. Banamine (flunixin meglumine, 2.5 mg/kg, subcutaneous) was given before and after the surgery, and again 3 days after cannula implantation.

Fluorescent tracers

10kDa-Dextran-FITC emerald (D1820, Thermo Scientific, US) was prepared in artificial CSF to a concentration of 0.5% w/v. Direct blue (DB53, E2129, Sigma-Aldrich, US) for intravenous injections was dissolved at 0.1% w/v in 0.9% sterile isotonic saline solution (Ricca Chemical Company, TX, US). For stereotaxic intraparenchymal delivery, a mixture of 0.25% w/v FITC (F2456, Sigma-Aldrich, US) and 0.25% (w/v) DB53 or 4% w/v DB53 in artificial CSF was used. For assessing effect of molecular size, either 4% w/v DB53 (0.96 kDa) or 4% w/v albumin coupled-DB53 (66.96 kDa) was used. To evaluate the feasibility of the assay with other compounds, two linear monofunctional PEG reagent, either with a fluorescein dye (FITC-PEG 1 kDa, PSB-2256, Creative PEGWorks, NC, USA) or a rhodamine dye (Rhodamine-PEG 40 kDa, PSB-2260, Creative PEGWorks, NC, USA) were used for either intravenous co-injections (DB53 and FITC-PEG 1kDa at 0.1% w/v each in sterile saline, 3 μ L, 0.2 μ L/min) or striatal injection co-injection (4% each w/v in sterile aCSF, 1 μ L, 0.2 μ L/min). For tracers, circulation time is defined as the time that the substance is moving freely after injection.

Intravenous injections

In anesthetized mice, the skin over the left femoral vein was opened, the vessels exposed. In the right femoral vein, an IV line (30G needle connected to PE10 tubing) filled with 0.1% DB53 or a mixture of DB53 and FITC-PEG 1kDa (0.1% w/v each), backfilled with mineral oil (to remove air and ensure accurate tracer delivery), connected to a 10 μ L syringe (1700 Gastight, Hamilton) was inserted. Using a syringe pump (Harvard Apparatus), tracers were injected into the vein as a bolus injection or at a rate of 0.2 μ L/min for 15 min. Autofluorescence at an unused channel (488 nm for DB53 and 555 nm for FITC-PEG 1kDa) was used to evaluate background prior to injection and during the whole experiment. FITC-PEG 1kDa and DB53 were imaged at 520 and 680 nm respectively. For urine DB53 or FITC-PEG 1kDa quantification, spectrophotometric signal was determined with a microplate reader at 520 or 620 nm (Model 680 Bio-Rad, Hercules, CA, USA), using a serial dilution standard curve to determine each tracer concentration.

Intracerebral cannula implant

Anesthetized mice were placed on a stereotaxic frame. The skin was opened, and a burr hole was drilled on the coordinates: AP +0.6 mm; ML - 2.0 mm (striatum) or AP +0.6 mm; ML - 1.2 mm (lateral ventricle), relative to bregma. After ensuring the meningeal layer break with a 30G needle, and either a guide cannula (26G, C315G SPC, 4.5 mm bellow pedestal) and dummy (33G, C315DC/SP, 0.1 mm projection) (chronic implants) (PlasticsOne, Roanoke, VA) or either only the inner infusion cannula (33G, C315I/SP, 0.1 mm projection, PlasticsOne, Roanoke, VA) was placed at DV -3.3 mm (striatum) or -2.0 mm (lateral ventricle) relative to bregma. For chronic implants, the incision was closed, and cannula secured via dental cement (Fisher Scientific, NC9991371).

Intra-striatal acute tracer injections

The cannula was attached to PE10 tubing connected to a 10 μ L Hamilton syringe containing a mixture of 0.25% FITC and 0.25% DB53 in sterile aCSF. After the end of the injection (1 μ L, 0.2 μ L/min), cannula was left in place for 5 min then removed slowly to avoid backflush. Skin over the incision was closed and animals were kept under anesthesia 30 min from the start of the infusion to allow intraparenchymal movement of the tracers (25 min of total circulation time). That time point was selected to isolate the intraparenchymal tracer dispersion, avoiding possible confusing effects caused by the efflux component, that should be limited at short times (Iliff et al., 2012, 2013a). Animals were killed by decapitation; their brains were quickly harvested and immediately vibratome fresh-sliced in ice-cold aCSF (300 μ m).

Representative slices separated 600 μm were placed in glass slides and imaged using a fluorescent macrocope (microscope: MVX10, Olympus; light: PRIOR Lumen 1600-LED; camera: Flash 4.0 digital, Hamamatsu). To help to minimize *ex vivo* diffusion, only one animal was processed at a time. As average, 30 min passed between the end of the circulation time and the end of the image acquisition.

Clearance assay

Animals were anesthetized, the dummy cannula was replaced by the inner cannula (33G, C315I/SP, 0.1 mm projection), connected by a PE10 tubing to a 10 μL Hamilton syringe containing 4% (w/v) DB53, 4% (w/v) albumin coupled-DB53 solution or 4% (w/v) FITC-PEG 1kDa in sterile aCSF. Mice were placed under a fluorescent macrocope (microscope: MVX10, Olympus; light: PRIOR Lumen 1600-LED; camera: Flash 4.0 digital, Hamamatsu) in the lateral position. The left femoral vein was exposed via skin resection and baseline images collected. It is important to note that opening the skin over the femoral vein is not needed to detect the DB53 signal (data not shown). We chose to expose the vessels to ensure consistent placement of the ROIs. The pump infusion (1 μL , 0.2 $\mu\text{L}/\text{min}$) was triggered simultaneously with the imaging over the vein, once every 15 min for 2 h for the intraparenchymal delivery. Exposed tissue was kept hydrated with 0.9% saline during the experiment. At the end of the experiment, animals were killed by decapitation and their brains were harvested for postmortem analysis. Data obtained from mice with incorrect cannula position were excluded.

Cisterna magna (CM) tracer injections

Anesthetized mice were fixed in a stereotaxic frame, the CM surgically exposed, and a 30 gauge needle connected to PE10 tubing filled with the tracer (10 kDa FITC-dextran or 4% (w/v) DB53 or albumin coupled-DB53) was inserted into the CM. Either 10 or 1 μL (10 kDa FITC-dextran or either DB53 solutions, respectively) of CSF tracer was infused at a rate of 2 or 0.2 $\mu\text{L}/\text{min}$ (FITC-Dextran or DB53 solutions) for five min with a syringe pump (Harvard Apparatus) (Iliff et al., 2012; Xavier et al., 2018). Animals were killed by decapitation and brains removed 30 min after the start of intracisternal infusion (note: the needle was left in place after infusion to prevent backflow of CSF).

For imaging of glymphatic influx, the brain was fixed overnight by immersion in 4% paraformaldehyde in PBS and subsequently, coronal vibratome slices (100 μm) were cut and mounted. Tracer influx into the brain was imaged *ex vivo* by macroscopic whole-brain (MVX10, Olympus) and whole-slice conventional fluorescence microscopy (montage epifluorescence microscope BX51 Olympus and CellSens Software), keeping constant exposure parameters. Tracer influx was quantified by a blinded investigator using FIJI (ImageJ) software as described previously (Hablitz et al., 2019; Iliff et al., 2012; Mestre et al., 2018a). The perimeter in each slice was manually outlined, and the mean fluorescence intensity within the ROIs was measured. An average of fluorescence intensity was calculated between six slices for a single animal, resulting in a single biological replicate. Equivalent slices were used for all biological replicates.

In vivo lymph node imaging

Anesthetized mice, with striatal cannula implanted, were placed in supine position under the macrocope (MVX10, Olympus) and skin over the neck was resected to show the superficial lymph nodes. Once exposed, a baseline image before the tracer infusion was taken ($t = 0$), and the pump was started (1 μL , 0.2 $\mu\text{L}/\text{min}$). Images at 488 and 620 nm were taken every 15 min for 120 min (ORCA Flash 4.0 CMOS Camera, Hamamatsu). Lymph nodes fluorescence was quantified at 680 nm by placing and ROI over their anatomical location, using the autofluorescence at 488 nm to ensure proper identification.

Intra-striatal PEG tracer co-injections

24-h striatal cannula implanted mice received a light dose of isoflurane (initial induction at 2%, maintained at 1 to 2% for the duration of the infusion). Then, the dummy cannula was replaced by the inner cannula (33G, C315I/SP, 0.1 mm projection), connected by a PE10 tubing to a 10 μL Hamilton syringe containing a mixture of 8% (w/v) FITC-PEG 1kDa and 8% (w/v) Rhodamine-PEG 40 kDa in sterile aCSF (final concentration of each, 4% (w/v)). Tracers were co-injected (1 μL , 0.2 $\mu\text{L}/\text{min}$) and the inner cannula was kept for 10 additional minutes to avoid backflush, before replacing it by the dummy cannula. Once the infusion was completed, animals were allowed to wake up and behave normally. For all the animals, tracers were infused at 12 pm (middle of the resting period) and samples were collected at 15 min (end of the infusion), 1h, 4h, 18h and 28h. At the required timepoints, animals were killed, and brains quickly collected over ice. Tracers were immediately extracted with formamide.

Immunohistochemistry

Quantitative immunohistochemistry on free floating sections analyzed immunolabeling for GFAP (MAB360, Millipore) and Iba1 (ab5076, Abcam). To suppress nonspecific binding, brain sections were incubated in 10% normal donkey serum-PBS containing 0.1% Triton X-100 and 0.2% gelatin for 1 h at room temperature. Incubations with primary antibodies (1:500) were carried out overnight at room temperature in PBS containing 5% normal donkey serum, 0.1% Triton X-100 and 0.2% gelatin followed by 3, 5-min washes in PBS. The sections were incubated with a secondary Cy3-conjugated donkey anti-mouse or goat (1:250; Jackson ImmunoResearch; catalog 711,165,151 and 705,165,147, respectively) antibody for 2 h at room temperature. The specificity of the immunostaining was tested by omitting the primary antibodies (data not shown).

The immunolabeled coronal slices were imaged using confocal microscopy (SP8, LASX software, 20x, Leica Microsystems, IL, US). Multichannel Z-stacks (20- μm , 1 μm step size) were acquired using the same acquisition parameters for all samples. Ipsi- and contra-lateral images were acquired in the same anatomical positions in both hemispheres in mice with cannula implantation.

Electroencephalogram recordings

Anesthetized animals were placed on a stereotaxic frame, where commercial telemetric electrodes (Pinnacle Technology, US) were implanted for electroencephalogram (EEG) recordings. The electrode plate was secured to the skull through EEG wire leads, inserted between the skull and underlying dura on small burr holes drilled in the skull 2.5 mm lateral and 2 mm posterior to bregma on left side of the midline. EEG leads were secured to the skull with dental acrylic and an electromyogram (EMG) lead was inserted in the neck muscles. Animals were kept under anesthesia and an additional burr hole was drilled to implant a guide cannula (26G, C315G SPC, 4.5 mm bellow pedestal) and dummy (33G, C315DC/SP, 0.1 mm projection) (PlasticsOne, Roanoke, VA) into the striatum (coordinates relative to bregma: AP +0.6 mm; ML - 2.0 mm; DV -3.25 mm). Animals were allowed to wake up and recover for 24 h.

On the experiment day, animals were anesthetized, placed over a 37°C temperature-controlled pad, and dummy replaced by the inner cannula (33G, C315I/SP, 0.1 mm projection) connected by a PE10 tubing to a 10 μL Hamilton syringe containing either 4% DB53 solution in sterile aCSF or sterile aCSF alone. First, the EEG and EMG were recorded for 20 min to establish baseline for each animal. Next, infusion with either aCSF or DB53 solution was performed (0.2 $\mu\text{L}/\text{min}$, 5 min) and additional 20 min recordings were acquired beginning at different timepoints (5-, 70- and 100-min post-injection). Signals were collected with Clampex 10.2 (sampling rate, 1000 Hz). EEG data were analyzed using a customized MATLAB script.

Size-selectivity efflux assessment

The initial solution (IS), a mixture of 40 $\mu\text{g}/\mu\text{L}$ DB53 (DB53, 0.9 kDa, E2129, Sigma-Aldrich, US) and 400 $\mu\text{g}/\mu\text{L}$ BSA (66 kDa, A8806, Millipore Sigma, US) in aCSF was incubated overnight at 37°C to allow complete binding. Next, 50 kDa cutoff Amicon Ultra-0.5 Centrifugal Filter Unit (UFC505024, Millipore Sigma, US) were used to elute the possible remaining free fraction of DB53 by centrifugation (30 min, 14,000g) (Filtered Solution 1, FS1). An additional volume of aCSF was added to draw out the remaining unbound DB53 and another round of centrifugation was performed (30 min, 14,000g) (Filtered Solution 2, FS2). The retained solution, containing DB53-BSA complexes with a molecular weight higher than 50 kDa, was recovered and reconstituted to the original volume (Bounded Solution, BS). Real concentration of 4% w/v DB53 in each solution and IS, FS1, FS2 and BS was spectroscopically determined at 680 nm using a microplate reader (Model 680 Bio-Rad, Hercules, CA, USA) at an excitation wavelength of 620 nm, using a serial dilution standard curve.

Formamide extraction

After intrastriatal or CM tracer injections, blood was collected through the inferior vena cava using a 24G IV catheter (Surflo SR-OX2419CA, Terumo, Somerset, NJ, USA) and 1 mL syringe (309,650, Becton& Dickinson, NJ, USA), previously heparinized, and transferred to EDTA-tubes (MiniCollect, 450,474, Greiner Bio-One, NC, USA) to avoid coagulation. Blood was centrifuged at 600 g for 10 min to precipitate blood cells and plasma was collected. 150 μL of plasma were mixed with 200 μL of formamide (11,814,320,001, Sigma-Aldrich, US). Immediately after blood collection, animals were transcardially perfused with PBS 0.1M to eliminate any blood present in the tissue, and brain and cervical lymph nodes were carefully dissected.

Forebrain was either separated in ipsilateral and contralateral sides (DB53) or kept intact (PEG co-injection) and each half was placed in 200 μL of aCSF, homogenized with a 150 Homogenizer (Fisher Scientific, PA, USA), and 1.8 mL of formamide (11,814,320,001, Sigma-Aldrich, US) were added. Metencephalon was dissected, weighed (W_{wet} , g) and dried at 65°C until constant weight was achieved (W_{dry} , g, ~ 48 h). The resulting water content ($W_{\text{wet}} - W_{\text{dry}} / W_{\text{dry}}$) was used to determine relation between dry and wet weight of the brain tissue (data not shown). Each of the lymph nodes were quantified individually.

All the tissue samples placed in formamide were incubated in a water bath at 55°C for 24 to 72h. At the end of the incubation period, samples were centrifuged at 16,000g for 20 min to precipitate any remaining tissue and the fluorescence of the supernatant was spectrophotometrically measured in a microplate reader at 485/538 nm (FITC-PEG 1kDa), 584/612 nm (Rhodamine-PEG 40 kDa) or 620/680 nm (DB53) (Model 680 Bio-Rad, Hercules, CA, USA), using a serial dilution standard curve to determine DB53 concentration.

Intracranial pressure (ICP) measurements

24h striatal cannula implanted WT or AQP4KO mice were anesthetized and placed in a stereotaxic frame and a 30-gauge needle cannula filled with aCSF was inserted into the CM (Xavier et al., 2018). Then, the same injection paradigm was used (1 μL , 0.2 $\mu\text{L}/\text{min}$) to inject aCSF in the striatum while ICP was monitored through the CM cannula connected to a transducer and a pressure monitor (BP-1, World Precision Instruments). ICP was acquired at 1 kHz, digitized, and monitored continuously for the duration of the infusion experiments with a DigiData 1550B digitizer and AxoScope software (Axon Instruments). Arterial blood pressure was measured through an arterial catheter placed in the femoral artery and connected to a pressure transducer and monitor (World Precision Instruments) and the same digitizer and recording equipment. Heart rate and respiratory rate were acquired at 1 kHz and 250 Hz, respectively, using a small animal physiological monitoring device (Harvard Apparatus).

Quantitative image analysis

All images were analyzed using ImageJ software (<https://imagej.nih.gov/ij/>). For *in vivo* femoral vein imaging: The fluorescence signal was calculated based on the mean pixel intensity in 8-bit images, acquired at the same magnification and exposure parameters, applying the same circular region of interest (ROI, 0.011 mm²). The anatomical details visualized by autofluorescence at 488 nm were used to confirm that the ROI was placed on top of femoral vein from beginning to end of the experiment. An identical ROI was placed in surrounding tissue (at least 1 mm away from the femoral vein, 0.011 mm²) to quantify background signal. To measure vessel diameter, the linear length was quantified with ImageJ, perpendicular to the vessel direction. Representative images are shown after flat field correction vs autofluorescence at 488 nm channel to eliminate reflected light artifacts. In all cases, overlay of 488 nm (gray) and 620 nm (blue, DB53) channel is shown. For *ex vivo* DB53 in the brain: The distribution of DB53 was assessed in coronal sections by determining the mean pixel intensity of 6 slices placed at 0.6 mm intervals along the brain, starting at bregma 1.2 mm. The average values from these representative 6 slices were used to compare DB53 from mouse to mouse. For *ex vivo* lymph node analysis: The mean pixel intensity was calculated for each lymph node, categorized by deep or superficial and ipsi- or contralateral anatomical position. If more than one lymph node was present at the same location, the average of their MPI was calculated. To evaluate the DB53 contribution to the signal in regard to tissue autofluorescence, same exposure images were acquired at 488 nm and 620/488 nm fluorescence MPI ratio was calculated.

Mathematical model

In our mathematical model, tracer is transported from the well-mixed injection site to the blood in two processes such that the mass m_i of DB53 at the injection site decreases in proportion to its concentration:

$$\frac{dm_i}{dt} = v_i \frac{dc_i}{dt} = - (q_1 + q_2) c_i(t).$$

Here t is time, v_i is the injection site volume, c_i is the concentration of DB53 in the injection site, and q_1 and q_2 are volume flow rates associated with two transport processes. The second transport process starts at time t_0 :

$$q_2 = \begin{cases} 0 & t < t_0 \\ q'_2 & t_0 \leq t \end{cases}$$

DB53 arrives in the blood at the same rate to conserve mass:

$$\frac{dm_b}{dt} = v_b \frac{dc_b}{dt} = (q_1 + q_2) c_i(t).$$

Here m_b is the mass of DB53 in the blood and v_b is the blood volume. Total mass is conserved according to $v_i c_i + v_b c_b = M$, where M is a constant. Combining algebraically and solving, we find that the blood concentration evolves according to

$$c_b = \begin{cases} C(1 - e^{-k_1 t}) & t < t_0 \\ C(1 - e^{-k_1 t_0} e^{-(k_1 + k'_2)(t - t_0)}) & \text{else} \end{cases}$$

Here $C = \frac{M}{v_b}$, $k_1 = q_1/v_i$, and $k'_2 = q'_2/v_i$.

Our data acquisition model assumes measured intensities are linearly related to the concentration (Figure 1), such that measured values are in proportion to DB53 concentration after baseline subtraction.

To estimate parameters, we minimized the squared error between the model predictions and the mean of each treatment group using Scipy (Virtanen et al., 2020) (after shifting their values to get baseline value of 0). R^2 was calculated as $1 - SS_R/SS_T$, where SS_T is total variation in the data and SS_R is variation in the residuals. Half-times were found by setting $c_b = \frac{C}{2}$ (half the equilibrium value C) and solving for t , finding therefore $T_{1/2} = \frac{\ln(2)}{q}$ (q being the rate in question).

QUANTIFICATION AND STATISTICAL ANALYSIS

When comparisons between different animals were done, experiments were performed in parallel. All statistical testing was performed on GraphPad Prism 8. Tests were chosen based on the dataset being analyzed and are reported in Tables S2 and S3. As common rule, Kolmogorov-Smirnov normality test was applied preceding further analysis to evaluate normality of the sample distribution; if not passed Mann-Whitney non-parametrical test was used. For comparing CL and IL sides of the brain paired t tests were used. To evaluate changes in fluorescence over the same mice ratio paired t tests were preferred, since ratios of differences were expected to be constant. For multiple comparisons, ordinary one-way ANOVA with Bonferroni's multiple comparisons test as Post Hoc test was preferred if the requirements for the analysis were met. In non-normal distributions, Kruskal-Wallis followed by Dunn's test as Post Hoc test was used. When the homoscedasticity assumption was not met, in normal data with non-equal SD, Brown-Forsythe and Tamhane's T2 multiple comparisons test as Post Hoc test was used. All statistical testing was 2 tailed, and exact p values were calculated at a 0.05 level of significance. All values are expressed as the mean \pm SD, and all the sample replicates are shown, unless otherwise stated. The significance levels were indicated as follows: * $p < 0.05$, ** $p < 0.01$, *** $p < 0.001$, **** $p < 0.0001$. Animal information and background values can be found in Table S1.